Title: Stimulated Raman Photothermal Microscopy towards Ultrasensitive Chemical Imaging

Authors: Yifan Zhu[1, #], Xiaowei Ge[2, #], Hongli Ni[2], Jiaze Yin[2], Haonan Lin[3], Le Wang[2], Yuying Tan[3], Chinmayee V. Prabhu Dessai[3], Yueming Li[4], Xinyan Teng[1], Ji-Xin Cheng[1,2,3,5, *]

Affiliations:

[1]Department of Chemistry, Boston University, Boston, MA, 02215, USA

[2]Department of Electrical and Computer Engineering, Boston University, Boston, MA, 02215, USA

[3]Department of Biomedical Engineering, Boston University, Boston, MA, 02215, USA

[4]Department of Mechanical Engineering, Boston University, Boston, MA, 02215, USA

[5]Photonics Center, Boston University, Boston, MA, 02215, USA

[#]Equal contribution

*Corresponding author: jxcheng@bu.edu

Abstract: Stimulated Raman scattering (SRS) microscopy has shown enormous potential in revealing molecular structures, dynamics and couplings in complex systems. However, the sensitivity of SRS is fundamentally limited to milli-molar level due to the shot noise and the small modulation depth. To overcome this barrier, we revisit SRS from the perspective of energy deposition. The SRS process pumps molecules to their vibrationally excited states. The thereafter relaxation heats up the surrounding and induces refractive index changes. By probing the refractive index changes with a laser beam, we introduce stimulated Raman photothermal (SRP) microscopy, where a >500-fold boost of modulation depth is achieved. Versatile applications of SRP microscopy on viral particles, cells, and tissues are demonstrated. SRP microscopy opens a way to perform vibrational spectroscopic imaging with ultrahigh sensitivity.

One-Sentence Summary: Stimulated Raman photothermal microscopy breaks the stimulated Raman scattering imaging detection limit.

INTRODUCTION

Avoiding the non-resonant background encountered in coherent anti-Stokes Raman scattering (CARS) microscopy, stimulated Raman scattering (SRS) microscopy has become a powerful platform in the field of chemical imaging (*1-3*). In SRS (**Fig. 1A**), two spatial-temporally overlapped laser pulse trains, namely pump and Stokes, coherently interact with Raman-active molecules that resonate at the laser beating frequency, causing a stimulated Raman gain and loss in the Stokes and the pump field, respectively. While providing the same molecular vibrational features as conventional Raman spectroscopy, SRS offers up to six orders of speed improvement comparing to spontaneous Raman (*3*). Such speed improvement, together with the development of vibrational probes (*4*), has enabled many applications, e.g. label-free stimulated Raman histology (*5,6*), nutrient mapping (*7-9*), unveiling altered metabolism in cancer (*10-14*), heterogeneity in the microbiome (*15*), rapid detection of antimicrobial susceptibility (*16*). Despite these advances, the detection sensitivity of SRS is fundamentally challenged by the small modulation depth (<0.1% for a pure liquid) and the shot noise in the pump or Stokes beam (*17,18*), where simply increasing the number of photons can easily exceed the power tolerance of the sample.

Pushing the fundamental limit of SRS sensitivity requires either a reduction of measurement noise or a boost of SRS signal. On the reduction of SRS measurement noise, efforts focused on using squeezed light, termed "quantum-enhanced SRS". Signal-to-noise-ratio (SNR) enhancements of 3.6 dB (*19*) with continuous wave squeezed light, or 2.89 dB (*20*) with pulsed squeezed light have been demonstrated with no additional perturbation on samples. While the future of this method is bright, it is currently limited by the low squeeze efficiency and decoherence in complex imaging systems. On the boost of SRS signal, different photophysical processes have been utilized to increase the cross-section, hence the signal intensity, including electronic pre-resonance SRS (*21-23*), plasmon-enhanced SRS (*24*) and stimulated Raman excited fluorescence (*25*). Very high enhancement factor ($10^4 \sim 10^7$) of SRS signal and single molecule SRS measurement (*24,25*) have been achieved. However, the requirement of special target molecules or plasmonic nanostructures constrains the scope of applications.

To seek approaches towards boosting the signal, we revisit the physics of SRS from the perspective of energy transfer from laser fields to the sample. As illustrated in **Fig. 1B**, when pump and Stokes pulses with appropriate wavelengths interact with Raman-active molecules, the target molecules are pumped to their vibrationally excited states, with the transition energy equals to the beating frequency between the pump and Stokes lasers. Importantly, after SRS excitation, the vibrationally excited molecules relax their vibrational energy quickly through non-radiative decay, and consequently, heat up the surrounding environment, causing a stimulated Raman photothermal (SRP) effect. As explored by Cheng and coworkers in 2007 from the perspective of photodamage in CARS imaging (*26*), ~0.08% of the laser power is absorbed by the myelin sample through the simultaneously occurring stimulated Raman gain and loss processes.

Optically detected photothermal microscopy has been well developed (*27*) and has reached the sensitivity down to a single molecule (*28*). In photothermal spectroscopy, first reported in the 1970s (*29*), an optical absorption raises the local temperature, creating a local change of refractive index, which is measured with a probing beam. Early photothermal microscopy works focused on electronic absorption, targeting non-fluorescent dye molecules or metal nanostructures (*27*). Recently developed mid-infrared photothermal (MIP) microscopy provides universal infrared active vibrational spectroscopic features, offers a detection sensitivity at micro-molar level, and creates a spatial resolution at the visible diffraction limit (*30,31*) or even higher by probing the high harmonic signals (*32*). On the contrary, the thermal effects induced by a Raman process are commonly believed to be minimal due to the small cross sections of Raman scattering. Here, we challenge this wisdom through low duty cycle coherent Raman excitation that nonlinearly benefits from high laser peak power. We show substantial thermal effect of an SRS process and demonstrate its potential in bond-selective imaging with ultrahigh sensitivity.

RESULTS

Simulation of the SRP effect

For a stimulated Raman loss measurement, the relationship between pump beam modulation depth η, pump laser intensity I_p, and change of photon number per pulse, ΔN, can be written as:

$$\eta = \frac{2 \cdot \Delta N \cdot \hbar\omega_p \cdot f_{rep}}{I_p} \tag{1}$$

where $\hbar$ is the reduced Plank's constant, ω_p is the angular frequency of the pump field, and f_{rep} is the laser repetition rate. With this, one can estimate the energy deposition per pair of SRS pulses by $E = \Delta N \cdot \hbar\omega_R$, where ω_R is the target Raman shift. Literature (*4*) has shown that with 25 mW (modulated at 50% duty cycle) and 15 mW on-sample powers for 80 MHz Stokes and pump beams, respectively, the SRS modulation depth on the 2913 cm^{-1} mode of dimethyl sulfoxide (DMSO) reaches 0.04%. By inserting these measured values into the equations, the energy deposition per pair of laser pulses is found to be 8.7 fJ, equivalent to 0.7 μW with 12.5 ns pulse spacing. This apparently large energy deposition agrees with Min's calculation of the apparent cross section of SRS (*33*).

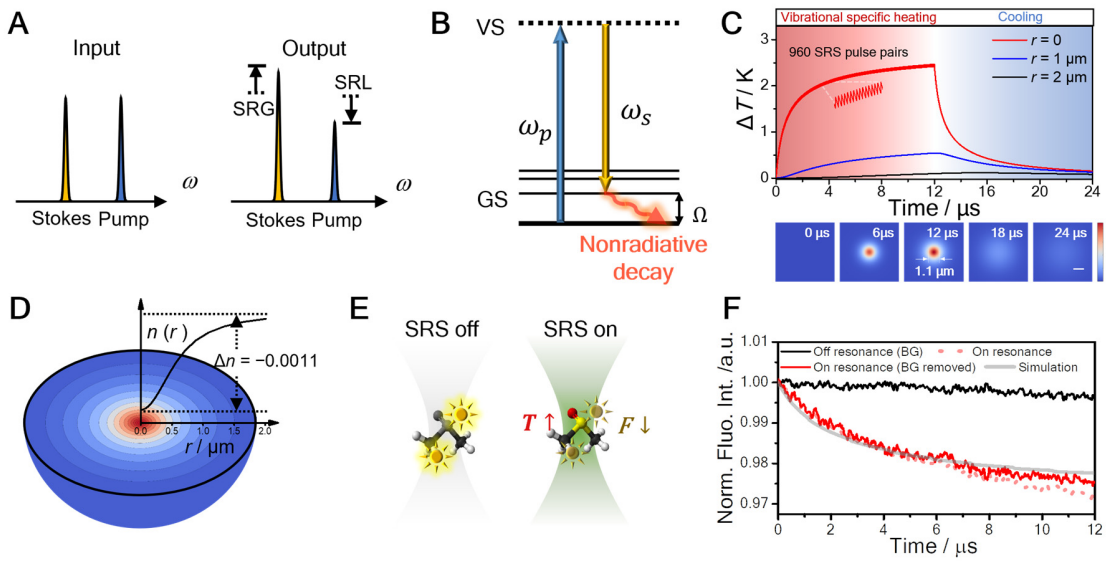

Fig. 1. Theoretical simulation and experimental observation of the SRP effect. (**A**) Schematic of stimulated Raman gain and loss. (**B**) Schematic of stimulated Raman photothermal (SRP) effect. (**C**) Simulation of temperature rise induced by SRP in temporal (top) and spatial (bottom) domains. Spatial scale bar: 1 μm. (**D**) Simulated profile of thermal lens induced by SRP in pure DMSO. (**E**) Illustration of fluorescence thermometer measurement of SRP-mediated temperature rise. (**F**) Fluorescence intensity of rhodamine B in DMSO during an SRS process. The beating frequency ($\omega_p - \omega_s$) is tuned to 2913 cm^{-1} for on resonance and 2850 cm^{-1} for off resonance. BG: background. The On resonance (BG removed) curve is obtained by subtracting the Off resonance (BG) from the on resonance curve, to eliminate the non-photothermal contributions.

With this energy deposition estimation, we applied Fourier's law and built a finite unit model (**Fig. S1**) to quantitatively simulate the stimulated Raman induced temperature rise in pure DMSO. Simulation results (**Fig. 1C**) show that, when using an objective with 0.8 NA (numerical aperture), and routinely used laser power for SRS (25 mW and 50 mW for pump and Stokes, 80 MHz repetition rate, 50% duty cycle), the temperature rise at the center of the laser focus can reach as high as 2.4 K after 12 μs of stimulated Raman excitation, corresponding to 960 pairs of pump/Stokes pulses. The temperature rises at r = 1 μm and 2 μm away from the focal center are 0.54 K and 0.12 K, respectively, at t = 12 μs. The temperature map at

different time points is also shown in **Fig. 1C**. The full width at half maximum (FWHM) of the temperature rising field at t = 12 μs is calculated to be 1.1 μm, suggesting a very localized thermal field.

The temperature elevation subsequently changes the local refractive index through the thermal-optic effect. For pure DMSO with a refractive index of 1.497 and a thermo-optic coefficient of -4.93×10^{-4} K^{-1} (dn/dT) (*34*), at t = 12 μs, the stimulated Raman induced heating causes a refractive index change by −0.07% at the focal center. As shown in **Fig. 1D**, such an index change nonlinearly extends to the surroundings through heat propagation, thus creating a thermal lens. The formation of such a thermal lens builds the foundation for SRP microscopy.

Experimental confirmation of the SRP effect

We experimentally confirmed the simulation results with a fluorescence thermometer. It has been well documented that the emission intensities of some fluorophores are temperature dependent (*35*). For instance, the fluorescence intensity of Rhodamine B decreases by ~2% per Kelvin at room temperature (*36*). This property has been utilized in fluorescence-detected mid-infrared photothermal spectroscopy (*37,38*). Here, we adopt this method to measure the temperature rise at the SRS focus, using Rhodamine B as a fluorescence thermometer. When the chirped pump and Stokes lasers are focused into a DMSO solution of Rhodamine B, the Rhodamine B molecules at the SRS focus are electronically excited through multiphoton absorption and emit fluorescence. Meanwhile, when the beating frequency between the pump and Stokes is tuned to resonate with the C-H vibration in DMSO, the SRP effect occurs to raise the temperature and accordingly decrease the two-photon fluorescence intensity of Rhodamine B molecules (**Fig. 1E**).

In the experiment, we used identical parameters as in the simulation. Firstly, the fluorescence intensity change curve measured at off-resonance frequency is subtracted from the on-resonance measurement to remove the photobleaching contribution in the result. Then, we found that the fluorescence intensity dropped ~2.3% after 12 μs of on-resonance SRS, corresponding to ~1.2 K of temperature rise (**Fig. 1F**), close to the simulation result of 2.4 K. The difference between the two values is majorly due to their different sampling region. The experiment measures the average temperature rise across the whole laser focus, while the simulation result shows only the temperature rise at the center of the laser focus (~20 nm diameter). After a weighted average of the temperature rises at different parts of the heating region, with consideration of corresponding two-photon excitation intensity of a Gaussian beam, the fluorescence change curve matches well the simulation curve, as shown in **Fig. 1F**.

To eliminate the potential impact of thermophoresis on the observed fluorescence intensity drop, we performed a control experiment using Rhodamine 800 (Rh800) as the dye in DMSO under the same SRS and two photon excitation schemes. The fluorescence of Rh800 is not temperature dependent, and not vulnerable to photobleaching. As shown in **Fig. S2**, the SRS process did not vary the Rh800 fluorescence intensity, indicating that thermophoresis played a negligible role.

Optically sensing the SRP effect

The SRP effect creates a divergent lens (**Fig. 1D**) and can be optically probed through a continuous wave beam. We built a thermal ball lens model to illustrate this detection scheme. In this model, we assume that SRS excitation creates uniform heating in a spherical symmetric region. Such a thermal ball-lens changes the subsequent probe light propagation, which is formulated based on geometrical optics (details in Supplementary Text and **Fig. S3**). Under the paraxial approximation, the model gives the proportionality of SRP signal intensity (I_{SRP}) induced by a single pair of pump and Stokes pulses as

$$I_{SRP} \propto N_{mol}\sigma_{SRS}I_{pump}I_{Stokes}\cdot\hbar\omega_{SRS}\cdot\frac{1}{V_{SRS}}\frac{1}{C_p n_0}\frac{dn}{dT} \quad (2)$$

Here, the first term ($N_{mol}\sigma_{SRS}I_{pump}I_{Stokes}$) describes the number of SRS events, i.e., the number of vibrational excitations, where N_{mol} is the number of molecule in the excitation volume, σ_{SRS} is the SRS cross section, and I_{pump} and I_{Stokes} are the intensity of pump and Stokes lasers, respectively. The second term ($\hbar\omega_{SRS}$) is the energy of vibrational transition. The last term describes properties of the measurement environment, where V_{SRS} is the SRS excitation volume, C_p is the heat capacity, n_0 is the refractive index, and $\frac{dn}{dT}$ is the thermo-optic coefficient. The product of the first and the second term gives the amount of energy deposition. The last term gives the rate of heat to refractive index conversion, which is inversely proportional to the excitation volume and the heat capacity and is linear to the thermo-optic coefficient. The environment properties term gives rise to the potential to improve the signal intensity, which is not applicable to SRS measurement. For the high numerical aperture (NA) condition, we carried out a finite-difference time-domain wave propagation simulation. The results (**Fig. S4**) show that the SRP signal maintains linearity to concentration.

An SRP microscope

By sensing the local refractive index modulation using a third continuous wave beam, we have built an SRP microscope as illustrated in **Fig. 2A**. Briefly, the synchronized pump and Stokes pulse trains are intensity-modulated by two acousto-optic modulators (AOM), combined, and chirped by glass rods. Here, chirping of femtosecond pulses generates spectral focusing for excitation of specific Raman modes (*39*,*40*). A probe beam is then collinearly aligned with the SRS beams. A pair of lenses adjusts the collimation of the probe beam to make the probe laser focus axially off the SRS focus, to maximize the photothermal signal (*27*). An iris at the back focal plane of the condenser lens is set to NA = 0.4 to convert the probe beam refraction modulation to intensity modulation. A fast photodiode detects the probe beam intensity, followed by a high pass filter and a broadband amplifier. The SRP modulation induced by synchronized pump and Stokes pulses is digitized in real time by a high-speed digitization card. Details can be found in Methods and **Fig. S5**.

Unlike SRS, both the pump and Stokes beam are intensity-modulated in the SRP microscope. Since the SRS intensity is proportional to the product of pump and Stokes peak power, with conserved average laser power, reduction of laser duty cycle leads to higher laser peak power, hence more SRS energy deposition. Our experiment (**Fig. 2B**) confirmed this idea and showed much higher SRP signal intensity with a lower duty cycle. In SRP imaging applications, the duty cycle was set to 5~10 % as a compromise between signal intensity and laser power. Notably, match filtering can be applied to the low duty cycle SRP signal to further improve the signal to noise ratio (**Fig. S6**). Another key parameter is the modulation frequency. Lower frequency shows higher signal intensity (**Fig. 2C**) due to longer heat accumulation time but suffers more from the 1/*f* laser intensity noise (*41*). Meanwhile, it reduces the imaging speed and compromises the spatial resolution. 125 kHz was chosen to balance these factors.

For pure liquid, under 5% duty cycle and 125 kHz modulation frequency, the induced modulation on the probe beam was so strong that we could directly measure the SRP signal in the direct current channel without any amplification, as shown in **Fig. 2D**. With reasonable laser powers on sample to excite the C-H symmetric stretching mode (2913 cm^{-1}) of DMSO, the modulation depth reached 22.3%, which is >500-fold higher than the SRS modulation depth (0.04%) with identical average power. The tremendously higher modulation depth builds the foundation for a better detection sensitivity.

In addition to duty cycle and modulation frequency, the thermal ball lens model shows that medium property is another crucial factor that affects the photothermal signal intensity. It agrees well with previous literature that the photothermal signal intensity (S), thermo-optic coefficient ($\frac{dn}{dT}$) and heat capacity (C_p) hold the relationship that $S \propto (\frac{dn}{dT}/C_p)$ (*42*). Yet, the most common medium in biological samples, i.e. water, has a relatively low thermo-optic coefficient (-1.13×10^{-4} K^{-1}) (*43*) and relatively high heat capacity (4181 $J\cdot kg^{-1}\cdot K^{-1}$). Seeking opportunities to increase the signal intensity, we investigated a few common

liquid media, as shown in **Table. S1**. We found that glycerol augments the signal intensity by 3.21 times compared to water. Meanwhile, glycerol shows high biocompatibility, and is widely used as a mounting medium or clearing agent in bio-imaging. Our simulation of the thermal lens comparison, shown in **Fig. S7**, also agrees with the previous theory that the peak refractive index change in glycerol medium is ~2.5-fold as high as in water, with identical heat source (100 nm poly(methyl methacrylate) PMMA nanoparticle under on-resonance SRP heating). Therefore, glycerol was chosen as the medium to push the sensitivity limit of SRP imaging. Considering the Raman-active vibrational features of glycerol itself, deuterated glycerol (glycerol-d8) was applied for SRP measurement at the C-H and fingerprint regions.

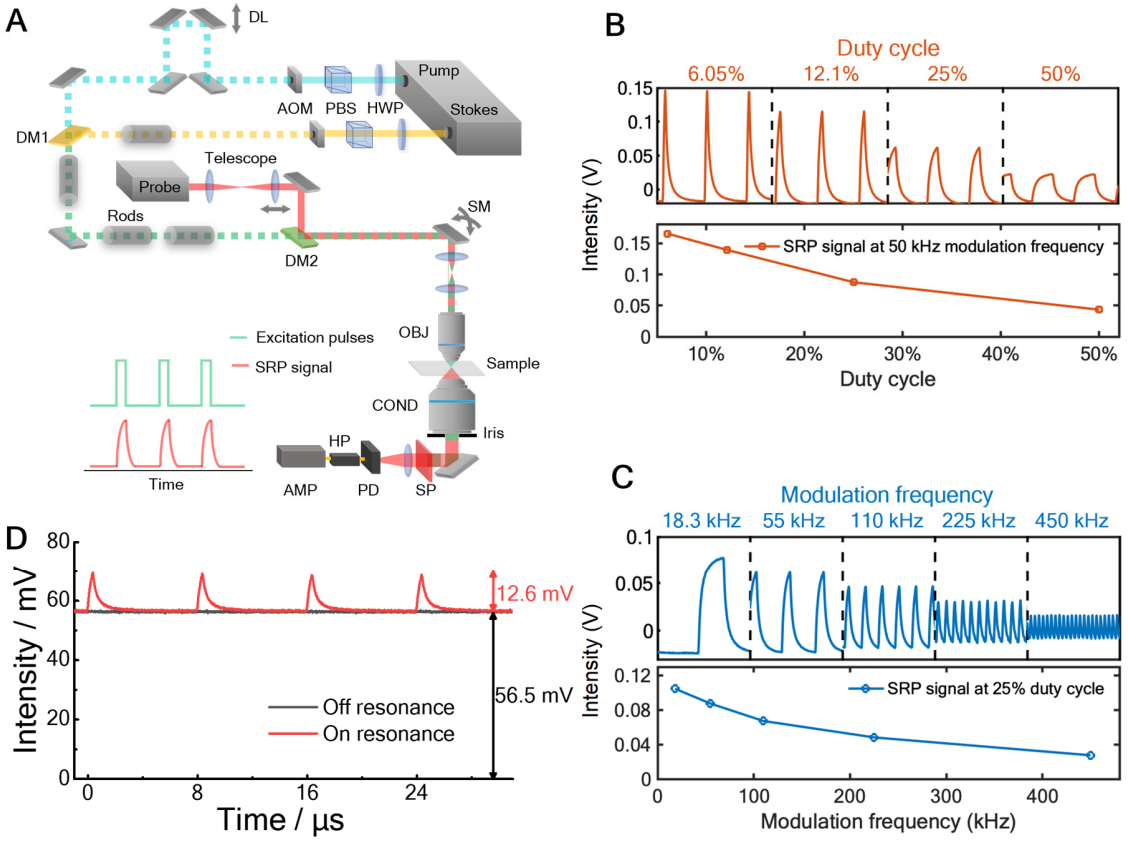

Fig. 2. SRP microscope design and characterization of SRP modulation depth as a function of duty cycle and modulation frequency. (**A**) Experimental setup. DM: dichroic mirror; DL: delay line; AOM: acousto-optic modulator; PBS: polarizing beam splitter; HWP: halfwave plate; SM: scanning mirror; OBJ: objective; COND: condenser; SP: spectral filter; PD: photodiode; HP: highpass filter; AMP: amplifier. (**B**) Measured SRP signal as a function of modulation duty cycle. (**C**) Measured SRP signal as a function of modulation frequency. (**D**) SRP generated a large (22.3%) modulation depth with DMSO as the sample. The on-resonance and off-resonance traces were obtained with the Raman shift at 2913 cm^{-1} and 2850 cm^{-1}, respectively.

SRP spectral fidelity and detection sensitivity

We first characterized the spectral fidelity of our SRP microscope with well-defined samples. As shown in **Fig. S8**, the SRP spectra show good agreement with SRS spectra for both bulk liquid sample and (PMMA) nanoparticles. We note that the SRP intensity is also proportional to ω_{SRS}, while its impact on the SRP spectrum is negligible in a narrow spectral window. The high spectral fidelity builds the foundation for us to further compare the detection sensitivity of the two techniques.

We then measured the limit of detection (LOD) for DMSO, focusing on the 2913 cm^{-1} mode. To keep the thermal and optical properties constant throughout the measurement, deuterated DMSO (DMSO-d6) was used as the solvent to dilute DMSO. As shown in **Fig. 3A** and **Fig. S9** (for complete measurement), the SRP spectrum was clean and smooth with a high concentration DMSO, and the signal was observable at a concentration as low as 5.1 mM. We calculated the LOD with the equation of LOD = $3\sigma/k$, where σ is the standard deviation of the baseline, and k is the slope of the intensity-concentration linear calibration curve. Calculation yielded an LOD value of 2.3 mM. In comparison, the LOD by SRS under identical average laser powers was found to be 39 mM. Thus, SRP measurement offers a ~17-fold improvement in LOD. The LODs for C≡C and C-D bonds were measured by using 1,7-Octadiyne in DMSO medium (**Fig. S10**) and DMSO-d6 in DMSO medium (**Fig. S11**). In both cases, SRP showed superior sensitivity than SRS with conserved average power, with 12-fold and 4-fold improvement of LOD, respectively.

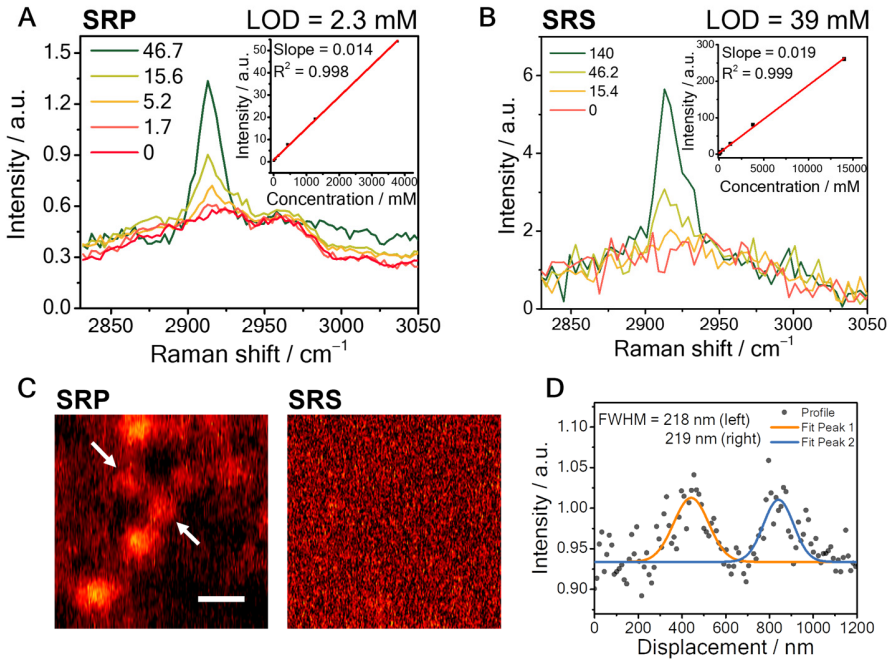

Fig. 3. SRP spectroscopy and imaging performance characterization. (**A-B**) SRP (**A**) or SRS (**B**) signal with gradient concentrations of DMSO dissolved in DMSO-d6. Concentration unit: mM. Insert shows the signal intensity as a function of concentration (complete data in **Fig. S6**). (**C**) SRP and SRS image of 100 nm PMMA beads at 2950 cm^{-1} with the same average power, at the same field of view. Scale bar: 500 nm. The beads were immersed in d8-glycerol. (**D**) The Gaussian fitting measured size of the bead is 218 nm (FWHM).

Such sensitivity improvement allows high-quality imaging of nanoparticles. With the SRP microscope, we successfully acquired a hyperspectral image of 100 nm PMMA beads as shown in **Fig. 3C**. The acquired SRP spectrum showed a Raman peak of PMMA at 2950 cm^{-1} which was well-distinguished from the background spectrum as shown in **Fig. S12**, with an SNR ~7.0 after BM4D denoising (*44*). In comparison, the SRS measurement showed no contrast of 100 nm beads on the same sample with identical average laser power. Collectively, SRP showed substantially improved sensitivity compared with SRS, both for liquid samples and for nanoparticles. Importantly, the introduction of a third probe beam at a shorter wavelength helped improve the spatial resolution (**Fig. 3D**). We plotted the intensity profile across a pair of 100 nm PMMA beads, with the Gaussian fitted FWHM found to be ~218 nm. Deconvolution with the size of the

beads generated an FWHM of ~ 194 nm, which was below the theoretical resolution limit of SRS under the same condition (~217 nm, FWHM of Airy disk).

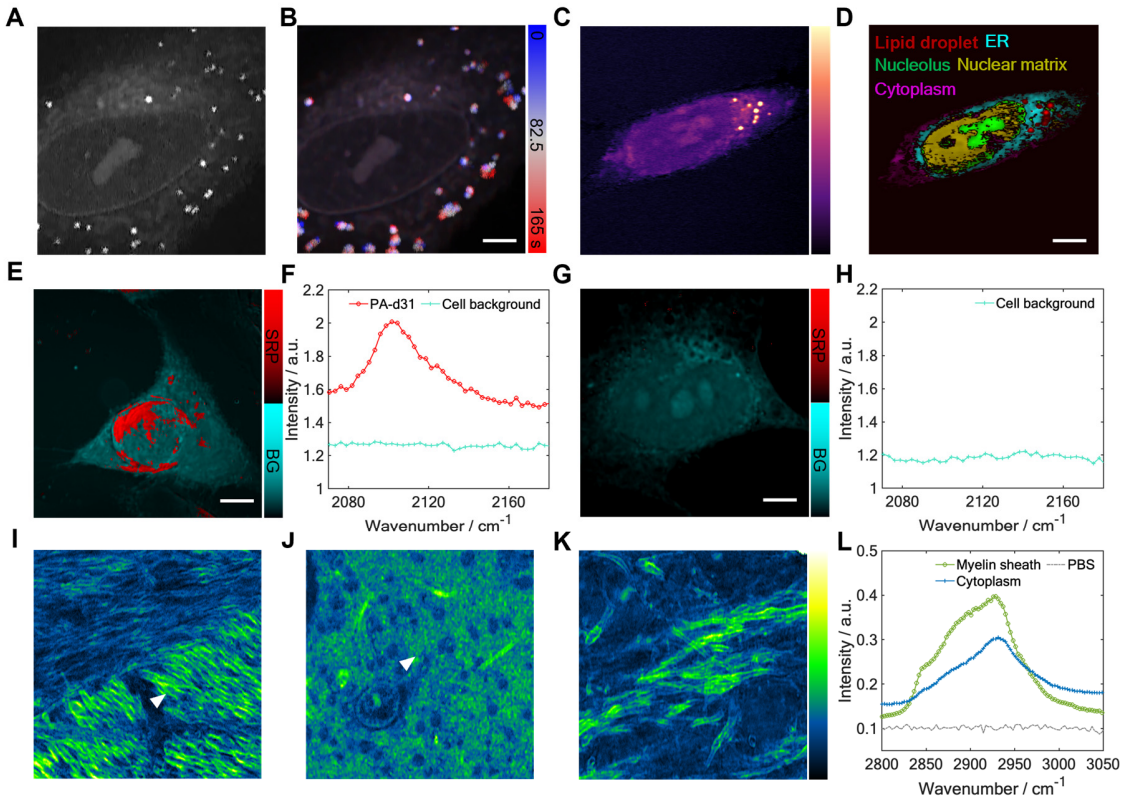

Fig.4 SRP imaging of biological samples in aqueous environment. (**A**) SRP image of a live SJSA-1 cell in PBS. Raman shift: 2930 cm^{-1}. (**B**) Dynamic imaging of the same live SJSA-1 cell with color coded temporal dynamics of the lipid droplets inside the cell. Scale bar: 5 µm. (**C**) Hyperspectral SRP imaging of fixed SJSA-1 cell in PBS, 2930 cm^{-1}. Scale bar: 10 µm. (**D**) Phasor analysis output of the hyperspectral SRP image in C. (**E-H**) SRP analysis of SJSA-1 cell in PBS with (**E**, **F**) or without (**G**, **H**) palmitic acid-d31 (PA-d31) treatment. Phasor analysis separates PA-d31 SRP signal (red) and cell background (cyan) (E, G) with spectral features shown in (F, H). Scale bar: 10 µm. (**I-K**) SRP imaging of a mouse brain immersed in PBS at 2930 cm^{-1} in different regions. Scale bar: 12 µm. (**L**) Two representative spectra in the mouse brain indicated with triangles in I (myelin sheath) and in J (cytoplasm). The PBS spectrum was acquired at the non-sample region.

SRP imaging of biological samples in physiological environment

To explore the potential of SRP in bio-imaging, we first performed label-free SRP imaging of live SJSA-1 osteosarcoma cancerous cells. As shown in **Fig. 4A**, the lipid droplets, Endoplasmic reticulum (ER) and nucleolus show strong signal at 2930 cm^{-1}. Nuclear membrane shows pronounced contrast, indicating a locally enhanced photothermal intensity in aqueous environment. At an imaging speed of ~2.8 s/frame, the dynamics of lipid droplets could be well captured, with all trajectories displayed in **Fig. 4B**. Complete time lapse movie is shown in **Movie S1**.

Next, we performed hyperspectral SRP imaging SJSA-1 cells at the C-H stretching vibration region. As demonstrated in **Fig. 4C**, the sub-cellular structures such as lipid droplets and nucleolus show decent

contrast. Subsequent phasor analysis was applied to segment the subcellular structures (*45*), where five of the major components are identified (**Fig. 4D**) with corresponding spectra (**Fig. S13**). Complete hyperspectral movie is shown in **Movie S2**.

To explore the applicability of SRP imaging to the silent window, we studied the cellular uptake of deuterated palmitic acid (PA-d31). **Fig. S14** shows the hyperspectral SRP images of SJSA-1 cells incubated with PA-d31. With phasor analysis, the PA-d31 rich regions, i.e. membrane and ER, can be well separated from other cellular components (**Fig. 4E**). The spectral profile (**Fig. 4F**) from phasor analysis shows a peak at 2100 cm^{-1}, where the C-D stretch vibration resides. In the control sample without PA-d31 treatment, only the cellular components were observed (**Fig. 4G, H**). It is worth noting that the background signal is independent of Raman shift (**Fig. 4F, H, Fig. S14**). This background is likely originated from the overtone absorption of C-H vibrational transitions, which also deposits energy and create photothermal contrast. The cell background in the C-D SRP images is stronger than that in the C-H SRP images (**Fig. 4D**), probably because the 855 nm pump laser used for C-D excitation is close to the 920 nm overtone absorption band of the C-H stretching vibration.

We then tested the SRP imaging performance for tissue specimens. We used mouse brain slice as the testbed (**Fig. 4I-K**). Three field-of-views (FOVs) are chosen as representations of typical brain structure. In **Fig. 4I,K**, rich and detailed structure of myelin sheath can be clearly resolved, showing typical lipid rich Raman spectral features on the spectrum. The myelin sheaths with different orientations show drastically different signal intensities, indicating a strong dependence of the SRP intensity on the laser polarization. In **Fig. 4J**, densely packed cytoplasmic organelles were observed. The SRP spectra (**Fig. 4L**) show lipid peak at 2845 cm^{-1} and protein peak at 2930 cm^{-1} for myelin sheath, while the cytoplasm signal is dominated by proteins. The SRP signal from the medium is weak and independent of Raman shift. Picture of the tissue sample and additional SRP tissue images are shown in **Fig. S15**. Collectively, our data show the potential of SRP imaging in chemical analysis of tissues with good spectral fidelity.

SRP imaging of biological samples in glycerol

Compared to water, the high thermo-optic coefficient and low heat capacity of glycerol open the opportunity to further boost the sensitivity of SRP microscopy. Inspired by the capability of imaging 100-nm nanoparticles with high SRP contrast (**Fig. 3C**), we first tested SRP imaging of individual viral particles. As shown in **Fig. 5A**, single varicella-zoster virus (diameter ≈ 180 nm) (*46*) could be clearly resolved from the background with an SNR ~20. The SRP spectrum of a single virus (**Fig. 5B**) peaked at 2950 cm^{-1}, indicating a strong contribution from the nucleotide at the core of the virus.

Glycerol-d8 as a mounting medium was used to improve the quality of SRP imaging of mammalian cells. We used pancreatic cancer cell MIA Paca-2 as the testbed (**Fig. 5C**). Glycerol-d8 was applied to replace the PBS buffer and immerse the cells to enhance the SRP contrast. SRP imaging at the high-wavenumber C-H vibration region shows high contrast from membranes and intracellular lipids. Phasor analysis was applied to segment the cellular compartments (**Fig. S16**), where up to six different components could be well identified (**Fig. 5D**). Notably, the nuclear membrane outstood from the cytoplasm and the nuclear matrix, giving rise to the potential of applying SRP to study fine structure in a membrane. The high contrast is probably due to the high thermo-optic coefficients and low heat capacities of membranes.

Upon addition of glycerol, the high sensitivity of SRP also provides access to weak Raman bands in the fingerprint region. **Fig. 5E** showed the SRP image of a 10 μm thick OVCAR-5 cancer tissue at 1650 cm^{-1}, targeting the Amide I band in proteins and the C=C vibration in lipids. High-quality spectra were resolved from the hyperspectral image stack. Lipid (region of interest 1 (ROI1)) and protein (ROI2) species are clearly differentiated, as shown in **Fig. 5F**.

Finally, we conducted a direct comparison between SRP and SRS at the same FOV on a SKOV3 cell in glycerol, with conserved average laser power and dwell time. The results are shown in **Fig. S17**. The representative cellular structures, e.g. lipid droplets, cell nuclear and nucleolus, can be clearly resolved in

both images. Comparison between profiles at the arrow-indicated lines on the 2980 cm^{-1} frames show a signal to noise ratio of 53 for SRP and 17 for SRS. Furthermore, the SRP image clearly shows sharper contrast for the intra-nuclear structures.

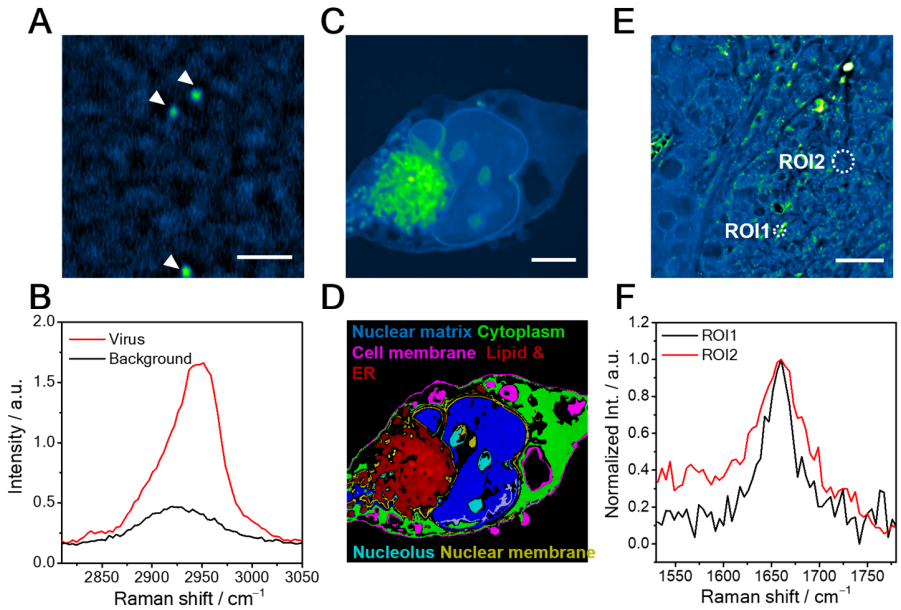

Fig. 5. SRP imaging of biological samples immersed in glycerol. (**A**) SRP imaging of a single varicella-zoster virus immersed in glycerol-d8, 2950 cm^{-1}. Scale bar: 2 µm. (**B**) Single virus Raman spectrum at C-H region, acquired from a single virus in **A**. (**C**) SRP imaging of fixed Mia-Paca2 cell immersed in glycerol-d8, at 2950 cm^{-1}. Scale bar: 5 µm. (**D**) Color coded chemical map through phasor analysis of **C**. (**E**) SRP spectroscopic imaging of OVCAR-5 tissue, cleared with glycerol-d8, at 1650 cm^{-1}. (**F**) Single pixel spectrum at the circled region of interests (ROI).

DISCUSSION

In this work, we have numerically simulated and experimentally confirmed the presence of SRP effect. Based on the SRP effect, we have built an SRP microscope, and demonstrated better detection sensitivity and resolution in comparison to a conventional SRS microscope. We have demonstrated SRP imaging of multiple biological samples in aqueous and glycerol environments. Below we compare SRP and SRS in terms of detection mechanism, spatial resolution, laser noise, and solvent effect.

SRS microscopy measures the gain in Stokes or the loss in the pump beam. Thus, a high-NA objective is needed to maximize the collection efficiency while minimizing the cross-phase modulation. On the contrast, SRP microscopy measures light refraction caused by the thermal lens. Thus, SRP favors light collection with a low-NA objective or an air condenser. As shown in **Fig. S18**, with a 0.5 NA air condenser, the SRP image is clear and sharp, while the SRS image is comparably noisier. Also, SRP maintains decent spectral fidelity (**Fig. S18C**), while SRS spectrum has been distorted by the enhanced cross phase modulation background. Quantitatively (**Fig. S18D**), the SRP image shows 21.2-fold SNR improvement and 7.8-fold SBR improvement comparing to SRS image. The relaxation of the requirement of high NA oil condenser brings convenience in the SRP applications.

SRP is slightly advantageous over SRS in term of spatial resolution. With the introduction of a probe laser, the ideal effective point spread function (PSF) is the product of all three laser PSFs (i.e. pump, Stokes and

probe). In addition, the probe can be chosen at a much shorter wavelength to yield a much sharper SRP effective PSF. In this work with a 1.49 NA objective, the ideal resolution reaches ~167 nm with a 765 nm laser applied as the probe, or ~137 nm when measured with a 522 nm laser. It is worth noting that, such ideal resolution improvement could be realized only with high frequency (>MHz), since thermal diffusion within a modulation period will enlarge the size of thermal lens, therefore compromises the resolution contribution from the probe beam. At the extreme of low modulation frequency, the resolution is degraded down to the SRS resolution. With current modulation frequency of 125 kHz, the spatial resolution improvement has been substantial (from SRS resolution of ~217 nm to SRP resolution of ~194 nm).

The different measurement scheme between SRP and SRS also brings different origin of noise in the measurement. In both measurements, the major origin of noise is the relative intensity noise and shot noise of the measured laser beam, which is the probe laser in SRP, or the pump/Stokes laser in SRS. The different origins of noise bring two advantages of SRP. First, SRP is immune to the laser noise of the ultrafast laser used for SRS excitation. Therefore, SRP can be implemented with a very noisy ultrafast laser; Second, both pump and Stokes laser powers can be increased without affecting the measurement noise of SRP. Therefore, SRP potentially enables the application of noisy and high-power lasers for vibrational imaging.

SRP is also distinct from SRS that the SRP signal is dependent on properties of the sample environment. As a result, the lipid-rich regions in the cellular images, such as lipid droplets and lipid bi-layers in membranes, show much enhanced contrast than in SRS images. This property also enables opportunities to greatly enhance the SRP signal intensity with carefully engineered medium, such as critical Xenon, which could bring a ~400-fold enhancement as demonstrated in visible photothermal microscopy (*27*). On the other side, the sample dependence of SRP signal may pose challenge to quantitative analysis in highly heterogeneous environments.

There is still space to further improve the SRP imaging performance. The imaging speed of our current setup can reach up to 8 us/pixel, or ~3 frame-per-second (FPS) for a 200×200 image. This imaging speed is majorly limited by the low modulation frequency at 125 kHz. It is possible to achieve much higher imaging speed by measuring the SRP effect caused by a single pair of SRS excitation pulses at 1 MHz repetition rate. Under such condition, the imaging speed is only constrained by the rate of sample cooling, usually on the level of 1 μs/pixel, which is sufficient for SRP imaging at close to video rate. Regarding the detection sensitivity, it is viable to incorporate more elegant photothermal detection scheme to boost the signal intensity, such as fluorescence detection (*37,38*) or nanomechanical photothermal sensing (*47*). Regarding spatial resolution, it is possible to switch to a shorter wavelength probe laser and couple with an imaging scanning microscopy technique (*48*) to further improve the resolution to sub-100-nm level.

MATERIALS AND METHODS

Cell culture and sample preparation

SKOV3 (Cat#: HTB-77) and Mia Paca2 (Cat#: CRL-1420) cells were from the American Type Culture Collection (ATCC). Cells were cultured in high-glucose DMEM medium (Gibco) supplemented with 10% FBS and 100 units/mL penicillin/streptomycin and maintained in a humidified incubator with 5% CO2 supply at 37°C. After overnight seeding in a sterile 35 mm glass-bottom dish (Cellvis) or #1 cover glass (VWR), cells were fixed with 10% neutral buffered formalin for 30 min followed by 3 times PBS wash. Then the cells were covered with glycerol-d8 before sealing and imaging.

SJSA-1 cells (Cat#: CRL-2098) were from the American Type Culture Collection (ATCC). Cells were cultured in RPMI-1640 culture medium (Gibco), supplemented with 10% (v/v) fetal bovine serum (FBS) and 1% (v/v) penicillin/streptomycin (P/S). All cells were cultured under controlled conditions in a humidified incubator set at 37 °C with a 5% CO2 supply. For the C-D labeled group, the cells were initially cultured until attaching to the glass bottom dishes, then incubated in RPMI-1640 medium containing de-lipid serum for 3 hours. Subsequently, the cells were incubated with 200 μM PA-d31 in the medium for 18

hours. Afterwards, cells were fixed with 10% neutral buffered formalin for 30 min followed by 3 times PBS wash before microscopic imaging.

Tissue sample preparation

OVCAR-cisR tissue sample: A fresh ovarian tumor section was extracted from NU/J mouse (4 weeks old female homozygous for Foxn1nu) purchased from the Jackson Laboratory. The mouse was inoculated with OVCAR5-cisR cells. The sections were immediately fixed in a 10% formalin solution. The extracted tissue section was then washed using PBS solution and cryopreserved by incubation in 15% sucrose solution for 12 hours, followed by incubation in 30% sucrose solution overnight at room temperature. The tissue section was frozen at −80°C by embedding in OCT (Optimal Cutting Temperature) compound in a tissue mold. The tissue section was then sliced using a Microm HM525 cryostat at the Bio-Interface and Technologies Facility, Boston University, into 10 µm thick layers, each placed on separate glass slides and frozen at −80°C until the experiment. To prepare the samples for imaging, the tissue slides were washed using PBS solution to wash off the OCT. The tissue slides were then covered with glycerol-d8 before placing a coverslip to seal the glycerol-d8 covered tissue layer.

Mouse brain tissue sample: The mouse were euthanized and perfused transcardially with phosphate-buffered saline (PBS, 1×, PH 7.4, Thermo Fisher Scientific Inc.) solution and 10% formalin, allowing the fixative to circulate throughout the vasculature. After fixation, the brain was extracted and fixed in 10% formalin solution for 24 h to ensure complete fixation. Then, the mouse brain was submerged in a 1× PBS solution and then sliced horizontally into sections with a thickness of 100 µm using an Oscillating Tissue Slicer (OST-4500, Electron Microscopy Sciences).

Glycerol-agar (glycerol-d8-agar) medium preparation

1% (w/w) agar (Sigma Aldrich) was mixed with glycerol (or glycerol-d8, Sigma Aldrich), then microwaved for 2min to fully dissolve the agar.

Nanoparticle, and virus preparation

For 100 nm PMMA nanoparticles, 10 µL solution was mixed with warm glycerol-d8-agar medium, then sandwiched between two No.1 coverslips before imaging. Varicella zoster virus solution (Fisher Scientific) was dropped onto a No.1 coverslip and dried on top. The sample was covered with glycerol-d8, then sandwiched between two coverslips and sealed with nail polish before imaging.

Modeling the temperature change induced by SRS

To quantitatively evaluate the SRP effect, we built a model to simulate the heat deposition spatially and temporally. The SRS induced temperature change is dependent on the pulse width, pulse energy, laser repetition rate, and thermal properties (thermal conductivity, heat capacity, etc.) of the sample and the surrounding medium. First, the deposited energy by SRS is estimated by the modulation depth on the pump or Stokes beam along with the pulse energy. Then, to simulate the thermal conduction, the time domain and spatial domain are divided into finite elements for the calculation according to Fourier's law: $dQ = -kA\,(dT/dr)$, where dQ is the conducted heat energy in the time window, k is the thermal conductivity, A is the surface area, dT is the temperature difference between distance dr. The SRS on-off process induces a heating and cooling process at the focus. Heat transfer happens during both heating and cooling. During the heating process, the SRS pulses deposit heat to the sample instantaneously with a Gaussian distribution as the vibrational excited state relaxation time is much faster compared to the simulation time grid. Finally, with the heating estimated by the modulation depth and the thermal conduction calculated according to Fourier's Law, the temperature spatial distribution at each time point is calculated.

To simplify the model, an isotropic Gaussian SRS heating area is assumed. The simulation area is set to be a 48-layer model with increasing step size from the center to the edge (**Fig. S1**). The time step is set to be 200 ps, which is much smaller than the heat propagation time to ensure a converged result. DMSO has a heat conductivity of 0.2 W/(m·K). The laser parameters are set to 50% duty cycle, 80 MHz repetition rate, according to the commonly used SRS setting.

To predict the fluorescence change upon temperature rise, the excitation profile of two photon fluorescence was modeled as the normalized Gaussian point spread function of the objective. Weights based on the assumed excitation profile were put onto the temperature rise of each layer, then multiplied by the −2%/K rate (*35*), to yield the fluorescence change.

Measurement of temperature at the SRS focus

A fluorescence thermometer, Rhodamine B (−2%/K) (*34*), is introduced to measure the temperature rise at the SRS focus. 80 μM Rhodamine B dissolved in DMSO is sandwiched between two thin coverslips (No.1; Thermo Fisher) for the measurement. A dual-output synchronized laser source (InSight X3; Spectra-Physics) provides pump and Stokes beams, respectively. The Stokes beam is modulated by an acousto-optic modulator (1205c; Isomet Corporation) at 40 kHz with the first order beam to provide a 100% modulation depth. Then the pump and Stokes beams are chirped by 75 and 90 cm glass rods (SF57; Scott AG), respectively, to implement hyperspectral SRS under a spectral focusing scheme. The path length of the Stokes beams could be adjusted by a motorized delay line (X-LRM025A-KX13A, Zaber Technologies). The two beams are combined by a dichroic mirror (950 nm; Chroma) and then collinearly guided into a laser scanning microscope. To vibrationally excite the C-H bond in DMSO, the pump laser was set to 800 nm with the Stokes beam wavelength fixed at 1045 nm. These two beams could also simultaneously excite the two-photon fluorescence signal of Rhodamine B. A 40× water objective (NA = 0.8); Olympus focused the two beams onto the sample, with power of 25 mW for pump and 50 mW for Stokes. The output light is collected in the forward direction by an oil condenser (NA = 1.4, Aplanat Achromat 1.4; Olympus) and a 75 mm A-coating focal lens (Thorlabs). A silicon photomultiplier (C14455-3050GA; Hamamatsu) module with a bandpass optical filter (RT570/20x; Chroma) and two short-pass filters (1000SP, 775SP; Thorlabs) is used to detect the fluorescence signal. The output of the silicon photomultiplier is recorded by a spectrometer (Moku:Lab, Liquid Instruments) for the analysis in **Fig. 1F**.

SRP microscope

The SRP microscope is based on the SRS setup described in the previous section. Both pump and Stokes beams are modulated by two synchronized acousto-optic modulators outputting the first order beams, various duty cycles, and modulation frequency at 125 kHz. Besides, a 765 nm continuous probe laser (TLB6712-D; Spectral Physics) is added after the combining dichroic mirror by a polarized beam splitter to form a three beam copropagating colinear system (**Fig. 2B**). The three beams are guided to a two-dimensional galvo scanning unit (GVS002; Thorlabs), which is conjugated by a four-focal system to the back aperture of a 100× oil objective (NA = 1.49, UAPON100XOTIRF; Olympus). The NA of the condenser is adjusted to 0.4 to enable the detection of the thermal lensing signal. The detector is a broadband silicon photodiode (Hamamatsu) with 50-ohm resistance, a 22 kHz highpass radio frequency filer (Mini-circuits) and a 46 dB low noise amplifier (SA230-F5; Wayne). A tilted bandpass optical filter (FL780-10; Thorlabs) is mounted before on the detector to block the SRS beams and allow sole detection of the probe beam. The output signal is digitized by a fast data acquisition card (Alazar card, ATS9462; Alazar Technologies). For the images of bio-samples in water environment (**Fig 4**), virus (**Fig 5A1**) and image comparison between SRS and SRP (**Fig. S17**), the 1045-nm femtosecond laser output is sent to an LBO crystal to generate 522.5 nm SHG laser beam and then chirped to serve as the SRP probe. This picosecond probe with reduced coherence length minimizes the interference from the medium/coverglass interface.

When performing SRS imaging on the same setup, the probe laser is turned off. A 1.4 NA condenser is used to minimize the cross phase modulation background. The modulation on the pump is set to always on and the Stokes was modulated at around 2.25 MHz. After the condenser, two short-pass optical filters (980SP, Thorlabs) pass the pump beam to the photodiode. A laboratory-built resonant amplifier after the photodiode picks up the stimulated Raman loss signal. The photodiode output is sent to the lock-in amplifier (MFLI; Zurich) and the stimulated Raman loss signal is recorded with a data acquisition card (NI DAQ card, PCI-6363; National Instruments). The SRS LOD measurements were performed on a separate SRS system with no modulation on pump, to ensure optimized measurement quality.

The SRP system is electronically synchronized by a NI DAQ card. The NI DAQ card controls the galvo scanning unit and generates the transistor-transistor logic trigger to control the sampling of the Alazar card and the pixel trigger to control the function generator. The function generator generates rectangular waves with various duty cycles at 125 kHz in burst mode to control the two acousto-optic modulators to modulate the pump and Stokes pulse trains (**Fig. S2**). The amplified signal from the detector set is digitized by the Alazar card at a sampling frequency of 20 MHz and then sent to the host computer for further analysis.

SRP signal digitization and processing

After recording the signal from each pixel, a Whittaker smoother removes the fluctuated baseline caused by variation in the transmission (*49*). Matched filtering is then applied to improve the SNR (*50*). Fourier transform on the baseline removed signal is applied to generate the signal spectrum. To reduce the out-of-frequency noise, a match multi-bandpass filter at up to seven harmonic frequencies of the modulation frequency is applied to the signal spectrum (**Fig. S6**). The width of the single bandpass filter is set to 13.89 kHz when the pixel dwell time is 72 µs. The match-filtered spectrum is then inversely Fourier transformed back to the time domain. The SPR signal intensity of each pixel is calculated from the average peak-dip contrast of the processed time domain data.

SRP imaging parameters

The modulation depth is measured with 5% duty cycle modulation, 50 mW and 20 mW for Stokes and pump, respectively. The virus image is acquired with 5% duty cycle modulation, 40 mW and 20 mW for Stokes and pump, respectively. The live cell image is acquired with 16 µs pixel integration time, and 10% duty cycle modulation, 40 mW and 20 mW for Stokes and pump, respectively. The glycerol-d8 mounted cell image is acquired with 10% duty cycle modulation, 30 mW and 15 mW for Stokes and pump, respectively. The tissue images are acquired with 5% duty cycle modulation, 30 mW and 10 mW for Stokes and pump, respectively. All powers are measured before the microscope.

Phasor analysis

Phasor analysis was performed with the standardized phasor analysis plug-in in ImageJ (1.49v). The phasor domain segmentation was performed manually to maximize the separation of different components as well as the integrity of each component.

Acknowledgements: We thank Dr. Hongjian He for the assistance in cell culture.

Funding: National Institutes of Health grant R35GM136223 (JXC)

Author contributions:

Conceptualization: J.X.C.
Methodology: Y.Z., X.G., H.N., H.L., L.W.
Software: Y.Z., J.Y.

Investigation: Y.Z., X.G.
Visualization: Y.Z., X.G.
Resources: Y.T., C.P.D, Y.L., X.T.
Supervision: J.X.C.
Writing—original draft: Y.Z., X.G.
Writing—review & editing: Y.Z., X.G., J.X.C.

Competing interests: J.X.C. declares financial interests in Vibronix Inc. and Photothermal Spectroscopy Corp., which did not fund the study. J.X.C, Y.Z., X.G., H.N., J.Y. are inventors of a patent application (U.S. Provisional No. 63/441,297), submitted by Boston University, that covers stimulated Raman photothermal microscopy. All other authors declare they have no competing interests.

Data and materials availability: All data needed to evaluate the conclusions in the paper are present in the paper and/or the Supplementary Materials. Raw data and code are available in Zenodo (DOI: 10.5281/zenodo.8141012).

References

1. C. W. Freudiger, W. Min, B. G. Saar, S. Lu, G. R. Holtom, C. He, J. C. Tsai, J. X. Kang, X. S. Xie, Label-free biomedical imaging with high sensitivity by stimulated Raman scattering microscopy. *Science*. **322**, 1857–1861 (2008).

2. W. Min, C. W. Freudiger, S. Lu, X. S. Xie, Coherent nonlinear optical imaging: beyond fluorescence microscopy. *Annu. Rev. Phys. Chem.* **62**, 507–530 (2011).

3. J.-X. Cheng, X. S. Xie, Vibrational spectroscopic imaging of living systems: An emerging platform for biology and medicine. *Science*. **350** (2015), doi:10.1126/science.aaa8870.

4. Z. Zhao, Y. Shen, F. Hu, W. Min, Applications of vibrational tags in biological imaging by Raman microscopy. *The Analyst*. **142**, 4018–4029 (2017).

5. M. Ji, D. A. Orringer, C. W. Freudiger, S. Ramkissoon, X. Liu, D. Lau, A. J. Golby, I. Norton, M. Hayashi, N. Y. R. Agar, G. S. Young, C. Spino, S. Santagata, S. Camelo-Piragua, K. L. Ligon, O. Sagher, X. S. Xie, Rapid, Label-Free Detection of Brain Tumors with Stimulated Raman Scattering Microscopy. *Sci. Transl. Med.* **5**, 201ra119-201ra119 (2013).

6. D. A. Orringer, B. Pandian, Y. S. Niknafs, T. C. Hollon, J. Boyle, S. Lewis, M. Garrard, S. L. Hervey-Jumper, H. J. L. Garton, C. O. Maher, J. A. Heth, O. Sagher, D. A. Wilkinson, M. Snuderl, S. Venneti, S. H. Ramkissoon, K. A. McFadden, A. Fisher-Hubbard, A. P. Lieberman, T. D. Johnson, X. S. Xie, J. K. Trautman, C. W. Freudiger, S. Camelo-Piragua, Rapid intraoperative histology of unprocessed surgical specimens via fibre-laser-based stimulated Raman scattering microscopy. *Nat. Biomed. Eng.* **1**, 0027 (2017).

7. F. Hu, Z. Chen, L. Zhang, Y. Shen, L. Wei, W. Min, Vibrational Imaging of Glucose Uptake Activity in Live Cells and Tissues by Stimulated Raman Scattering. *Angew. Chem. Int. Ed.* **54**, 9821–9825 (2015).

8. L. Shi, C. Zheng, Y. Shen, Z. Chen, E. S. Silveira, L. Zhang, M. Wei, C. Liu, C. de Sena-Tomas, K. Targoff, W. Min, Optical imaging of metabolic dynamics in animals. *Nat. Commun.* **9**, 2995 (2018).

9. J. Li, J.-X. Cheng, Direct visualization of de novo lipogenesis in single living cells. *Sci. Rep.* **4**, 6807 (2014).

10. S. Yue, J. Li, S.-Y. Lee, H. J. Lee, T. Shao, B. Song, L. Cheng, T. A. Masterson, X. Liu, T. L. Ratliff, J.-X. Cheng, Cholesteryl Ester Accumulation Induced by PTEN Loss and PI3K/AKT Activation Underlies Human Prostate Cancer Aggressiveness. *Cell Metab.* **19**, 393–406 (2014).

11. J. Du, Y. Su, C. Qian, D. Yuan, K. Miao, D. Lee, A. H. C. Ng, R. S. Wijker, A. Ribas, R. D. Levine, J. R. Heath, L. Wei, Raman-guided subcellular pharmaco-metabolomics for metastatic melanoma cells. *Nat. Commun.* **11**, 4830 (2020).

12. H. J. Lee, Z. Chen, M. Collard, F. Chen, J. G. Chen, M. Wu, R. M. Alani, J.-X. Cheng, Multimodal Metabolic Imaging Reveals Pigment Reduction and Lipid Accumulation in Metastatic Melanoma. *BME Front.* **2021**, 1–17 (2021).

13. C. Chen, Z. Zhao, N. Qian, S. Wei, F. Hu, W. Min, Multiplexed live-cell profiling with Raman probes. *Nat. Commun.* **12**, 3405 (2021).

14. Y. Tan, J. Li, G. Zhao, K.-C. Huang, H. Cardenas, Y. Wang, D. Matei, J.-X. Cheng, Metabolic reprogramming from glycolysis to fatty acid uptake and beta-oxidation in platinum-resistant cancer cells. *Nat. Commun.* **13**, 4554 (2022).

15. X. Ge, F. C. Pereira, M. Mitteregger, D. Berry, M. Zhang, B. Hausmann, J. Zhang, A. Schintlmeister, M. Wagner, J.-X. Cheng, SRS-FISH: A high-throughput platform linking microbiome metabolism to identity at the single-cell level. *Proc. Natl. Acad. Sci. U. S. A.* **119**, e2203519119 (2022).

16. M. Zhang, W. Hong, N. S. Abutaleb, J. Li, P.-T. Dong, C. Zong, P. Wang, M. N. Seleem, J.-X. Cheng, Rapid Determination of Antimicrobial Susceptibility by Stimulated Raman Scattering Imaging of D2O Metabolic Incorporation in a Single Bacterium. *Adv. Sci. Weinh. Baden-Wurtt. Ger.* **7**, 2001452 (2020).

17. W. Rock, M. Bonn, S. H. Parekh, Near shot-noise limited hyperspectral stimulated Raman scattering spectroscopy using low energy lasers and a fast CMOS array. *Opt. Express*. **21**, 15113–15120 (2013).

18. C.-S. Liao, M. N. Slipchenko, P. Wang, J. Li, S.-Y. Lee, R. A. Oglesbee, J.-X. Cheng, Microsecond scale vibrational spectroscopic imaging by multiplex stimulated Raman scattering microscopy. *Light Sci. Appl.* **4**, e265–e265 (2015).

19. R. B. de Andrade, H. Kerdoncuff, K. Berg-Sørensen, T. Gehring, M. Lassen, U. L. Andersen, Quantum-enhanced continuous-wave stimulated Raman scattering spectroscopy. *Optica*. **7**, 470–475 (2020).

20. Z. Xu, K. Oguchi, Y. Taguchi, S. Takahashi, Y. Sano, T. Mizuguchi, K. Katoh, Y. Ozeki, Quantum-enhanced stimulated Raman scattering microscopy in a high-power regime. *Opt. Lett.* **47**, 5829–5832 (2022).

21. L. Wei, Z. Chen, L. Shi, R. Long, A. V. Anzalone, L. Zhang, F. Hu, R. Yuste, V. W. Cornish, W. Min, Super-multiplex vibrational imaging. *Nature*. **544**, 465–470 (2017).

22. L. Wei, W. Min, Electronic Preresonance Stimulated Raman Scattering Microscopy. *J. Phys. Chem. Lett.* **9**, 4294–4301 (2018).

23. M. Zhuge, K.-C. Huang, H. J. Lee, Y. Jiang, Y. Tan, H. Lin, P.-T. Dong, G. Zhao, D. Matei, Q. Yang, J.-X. Cheng, Ultrasensitive Vibrational Imaging of Retinoids by Visible Preresonance Stimulated Raman Scattering Microscopy. *Adv. Sci. Weinh. Baden-Wurtt. Ger.* **8**, 2003136 (2021).

24. C. Zong, R. Premasiri, H. Lin, Y. Huang, C. Zhang, C. Yang, B. Ren, L. D. Ziegler, J.-X. Cheng, Plasmon-enhanced stimulated Raman scattering microscopy with single-molecule detection sensitivity. *Nat. Commun.* **10**, 5318 (2019).

25. H. Xiong, L. Shi, L. Wei, Y. Shen, R. Long, Z. Zhao, W. Min, Stimulated Raman excited fluorescence spectroscopy and imaging. *Nat. Photonics*. **13**, 412–417 (2019).

26. H. Wang, Y. Fu, J.-X. Cheng, Experimental observation and theoretical analysis of Raman resonance-enhanced photodamage in coherent anti-Stokes Raman scattering microscopy. *J. Opt. Soc. Am. B*. **24**, 544 (2007).

27. S. Adhikari, P. Spaeth, A. Kar, M. D. Baaske, S. Khatua, M. Orrit, Photothermal Microscopy: Imaging the Optical Absorption of Single Nanoparticles and Single Molecules. *ACS Nano*. **14**, 16414–16445 (2020).

28. A. Gaiduk, M. Yorulmaz, P. V. Ruijgrok, M. Orrit, Room-Temperature Detection of a Single Molecule's Absorption by Photothermal Contrast. *Science*. **330**, 353–356 (2010).

29. M. E. Long, R. L. Swofford, A. C. Albrecht, Thermal Lens Technique: A New Method of Absorption Spectroscopy. *Science*. **191**, 183–185 (1976).

30. D. Zhang, C. Li, C. Zhang, M. N. Slipchenko, G. Eakins, J.-X. Cheng, Depth-resolved mid-infrared photothermal imaging of living cells and organisms with submicrometer spatial resolution. *Sci. Adv.* **2**, e1600521 (2016).

31. Z. Li, K. Aleshire, M. Kuno, G. V. Hartland, Super-Resolution Far-Field Infrared Imaging by Photothermal Heterodyne Imaging. *J. Phys. Chem. B*. **121**, 8838–8846 (2017).

32. P. Fu, W. Cao, T. Chen, X. Huang, T. Le, S. Zhu, D.-W. Wang, H. J. Lee, D. Zhang, Super-resolution imaging of non-fluorescent molecules by photothermal relaxation localization microscopy. *Nat. Photonics*, 1–8 (2023).

33. X. Gao, X. Li, W. Min, Absolute Stimulated Raman Cross Sections of Molecules. *J. Phys. Chem. Lett.* **14**, 5701–5708 (2023).

34. H. El-Kashef, The necessary requirements imposed on polar dielectric laser dye solvents—II. *Phys. B Condens. Matter*. **311**, 376–379 (2002).

35. E. J. Bowen, J. Sahu, The Effect of Temperature on Fluorescence of Solutions. *J. Phys. Chem.* **63**, 4–7 (1959).

36. A. Soleilhac, M. Girod, P. Dugourd, B. Burdin, J. Parvole, P.-Y. Dugas, F. Bayard, E. Lacôte, E. Bourgeat-Lami, R. Antoine, Temperature Response of Rhodamine B-Doped Latex Particles. From Solution to Single Particles. *Langmuir*. **32**, 4052–4058 (2016).

37. M. Li, A. Razumtcev, R. Yang, Y. Liu, J. Rong, A. C. Geiger, R. Blanchard, C. Pfluegl, L. S. Taylor, G. J. Simpson, Fluorescence-Detected Mid-Infrared Photothermal Microscopy. *J. Am. Chem. Soc.* **143**, 10809–10815 (2021).

38. Y. Zhang, H. Zong, C. Zong, Y. Tan, M. Zhang, Y. Zhan, J.-X. Cheng, Fluorescence-Detected Mid-Infrared Photothermal Microscopy. *J. Am. Chem. Soc.* **143**, 11490–11499 (2021).

39. T. Hellerer, A. M. K. Enejder, A. Zumbusch, Spectral focusing: High spectral resolution spectroscopy with broad-bandwidth laser pulses. *Applied Physics Letters*. **85**, 25–27 (2004).

40. D. Fu, G. Holtom, C. Freudiger, X. Zhang, X. S. Xie, Hyperspectral Imaging with Stimulated Raman Scattering by Chirped Femtosecond Lasers. *J. Phys. Chem. B*. **117**, 4634–4640 (2013).

41. C. W. Freudiger, W. Yang, G. R. Holtom, N. Peyghambarian, X. S. Xie, K. Q. Kieu, Stimulated Raman scattering microscopy with a robust fibre laser source. *Nat. Photonics*. **8**, 153–159 (2014).

42. A. Gaiduk, P. V. Ruijgrok, M. Yorulmaz, M. Orrit, Detection limits in photothermal microscopy. *Chem. Sci.* **1**, 343–350 (2010).

43. S. Novais, M. S. Ferreira, J. L. Pinto, Determination of thermo-optic coefficient of ethanol-water mixtures with optical fiber tip sensor. *Opt. Fiber Technol.* **45**, 276–279 (2018).

44. M. Maggioni, V. Katkovnik, K. Egiazarian, A. Foi, Nonlocal transform-domain filter for volumetric data denoising and reconstruction. *IEEE Trans. Image Process. Publ. IEEE Signal Process. Soc.* **22**, 119–133 (2013).

45. D. Fu, X. S. Xie, Reliable Cell Segmentation Based on Spectral Phasor Analysis of Hyperspectral Stimulated Raman Scattering Imaging Data. *Anal. Chem.* **86**, 4115–4119 (2014).

46. A. Sauerbrei, Diagnosis, antiviral therapy, and prophylaxis of varicella-zoster virus infections. *Eur. J. Clin. Microbiol. Infect. Dis. Off. Publ. Eur. Soc. Clin. Microbiol.* **35**, 723–734 (2016).

47. M.-H. Chien, M. Brameshuber, B. K. Rossboth, G. J. Schütz, S. Schmid, Single-molecule optical absorption imaging by nanomechanical photothermal sensing. *Proceedings of the National Academy of Sciences*. **115**, 11150–11155 (2018).

48. E. n. Ward, R. Pal, Image scanning microscopy: an overview. *Journal of Microscopy*. **266**, 221–228 (2017).

49. P. H. C. Eilers, A perfect smoother. *Anal. Chem.* **75**, 3631–3636 (2003).

50. J. Yin, L. Lan, Y. Zhang, H. Ni, Y. Tan, M. Zhang, Y. Bai, J.-X. Cheng, Nanosecond-resolution photothermal dynamic imaging via MHZ digitization and match filtering. *Nat. Commun.* **12**, 7097 (2021).

51. Bialkowski, S. E., "Photothermal spectroscopy methods for chemical analysis", Vol. 134 of *Chemical Analysis: A Series of Monographs on Analytical Chemistry and Its Applications*, J. D. Winefordner, ed., (John Wiley & Sons, Inc., 1996), pp. 290.

52. Z. Cao, L. Jiang, S. Wang, M. Wang, D. Liu, P. Wang, F. Zhang, Y. Lu, All-glass extrinsic Fabry-Perot interferometer thermo-optic coefficient sensor based on a capillary bridged two fiber ends. *Appl. Opt.* **54**, 2371–2375 (2015).

53. Z. Zhang, P. Zhao, P. Lin, F. Sun, Thermo-optic coefficients of polymers for optical waveguide applications. *Polymer*. **47**, 4893–4896 (2006).

Science
AAAS

Supplementary Materials for

Stimulated Raman Photothermal Microscopy towards Ultrasensitive Chemical Imaging

Yifan Zhu, Xiaowei Ge, Hongli Ni, Jiaze Yin, Haonan Lin, Le Wang, Yuying Tan, Chinmayee V. Prabhu Dessai, Yueming Li, Xinyan Teng, Ji-Xin Cheng*

*Correspondence to: jxcheng@bu.edu

This PDF file includes:

Supplementary Text
Figs. S1 to S17
Table S1
Captions of Movies S1 and S2

Other Supplementary Material for this manuscript includes the following:

Movies S1 and S2

Supplementary Text

The SRP Ball lens model

The number of SRS events (N_{SRS}) induced by a single pair of pump and Stokes pulses is given by:

$$N_{SRS} = N_{mol} \cdot \sigma_{SRS} \cdot I_{pump} \cdot I_{Stokes} \quad (S1)$$

Where N_{mol} is the number of Raman active chemical bond in the laser focus, σ_{SRS} is the Raman cross-section, I_{pump} and I_{Stokes} are the intensity of pump and Stokes lasers, respectively.

The energy deposition (Q) through SRS process is then given by:

$$Q = \hbar\omega_{SRS} \cdot N_{SRS} \quad (S2)$$

Where $\hbar$ is the reduced Planck constant, ω_{SRS} is the Raman transition energy. This energy deposition causes a temperature rise (ΔT)

$$\Delta T = \frac{Q}{C_p \cdot V_{SRS}} \quad (S3)$$

Where C_p is the heat capacity of the medium, and V_{SRS} is the volume of the SRS excitation.

The elevated temperature then changes the refractive index of the medium (Δn):

$$\Delta n = \Delta T \cdot \frac{dn}{dT} \quad (S4)$$

Where dn/dT is the thermos-optic coefficient of the medium.

As shown in Figure S4, the changed refractive index effectively forms a thermal ball lens, with its focal length f satisfies that:

$$\frac{1}{f} = \frac{2}{r}\left(\frac{n_1}{n_0} - 1\right) = \frac{2\Delta n}{n_0 r} \quad (S5)$$

Here, r is the radius of the ball-lens, n_0 is the refractive index of the medium, n_1 is the refractive index of the ball-lens.

To probe the thermal lens effect, we introduce a focused Gaussian probe laser that is collinear with the laser beams for SRS. The ball-lens changes the propagation of the probe light, with dashed line indicating the light propagation without ball lens, and solid line indicating light propagation with ball lens:

$$\frac{1}{f} = \frac{1}{q} - \frac{1}{z_f} \quad (S6)$$

Where z_f denotes the offset between the SRS and probe laser focus.

Under paraxial approximation, for an annular ray of light with incident angle θ as shown in **Fig. S3**, Eq. (S6) becomes:

$$\frac{1}{f} \approx \frac{\Delta\Theta(\theta)}{z_f sin\theta cos\theta} \quad (S7)$$

Here, $\Delta\Theta(\theta)$ is the change of propagation angle of the probe light at angle θ.

Combining Eq. (S5) and Eq. (S7) yields the change of laser propagation angle $\Delta\Theta$ induced by the ball lens as a function of incident angle θ:

$$\Delta\Theta(\theta) = \frac{2z_f \cdot \Delta n \cdot sin\theta cos\theta}{n_0 r} \quad (S8)$$

The far-field annular intensity distribution of the probe laser, $I(\theta)$, can be written as

$$I(\theta) = I_0 \pi Z_R^2 \cdot \theta \cdot \exp\left(-\frac{Z_R^2}{\omega_0^2} \cdot \theta^2\right) \quad (S9)$$

where Z_R is the Rayleigh length of the laser focus, and ω_0 is the beam waist. After propagating through the ball lens, the probe laser intensity is measured by a photodetector with angular detection aperture size θ_{Det}. Thus, the SRP signal is calculated as the intensity difference with the presence or absence of the ball lens:

$$I_{SRP} = \int_0^{\theta_{Det}} I\big(\theta + \Delta\Theta(\theta)\big)\, d\theta - \int_0^{\theta_{Det}} I(\theta)\, d\theta \approx I(\theta_{Det}) \cdot \Delta\Theta(\theta_{Det}) \quad (S10)$$

Combining all above equations gives:

$$I_{SRP} \approx I(\theta_{Det}) \frac{4z_f \cdot sin\theta_{Det} \cdot cos\theta_{Det}}{n_0 r} \cdot \frac{1}{C_p} \frac{dn}{dT} \cdot \frac{1}{V_{SRS}} \cdot (\hbar\omega_{SRS})\,(N_{mol}\sigma_{SRS} I_{pump} I_{Stokes}) \quad (S11)$$

In Eq. (S11), $\frac{1}{C_p}\frac{dn}{dT}$ denotes the thermal and thermos-optic properties of the sample environment. V_{SRS} denotes the volume of heating. $\hbar\omega_{SRS}$ represents the energy of vibrational transition. $N\sigma_{SRS} I_{pump} I_{Stokes}$ represents the number of transitions caused by SRS.

Under the tight focusing condition, a FDTD Simulation is carried out to calculate the dependence of SRP intensity on the molecular concentration. First, a thermal ball-lens model is generated in MATLAB as a matrix, where the refractive index outside the ball-lens is set to the refractive index of the DMSO medium (n_0 = 1.4793), and the refractive index inside ball-lens region is set to different lower values ($n = n_0 - \Delta n$; Δn is the refractive index change). Then, the thermal ball-lens model is imported to FDTD as a "(n,k) material" object. A Gaussian focused light source is sent through the thermal ball-lens object and measured with a far-field intensity analyzer, of which the output is a far-field angular distribution of intensity. The middle 31° (~0.4 numerical aperture) of the angular distribution of intensity is integrated, then subtracted by the corresponding 0-concentration value to get the SRP signal intensity.

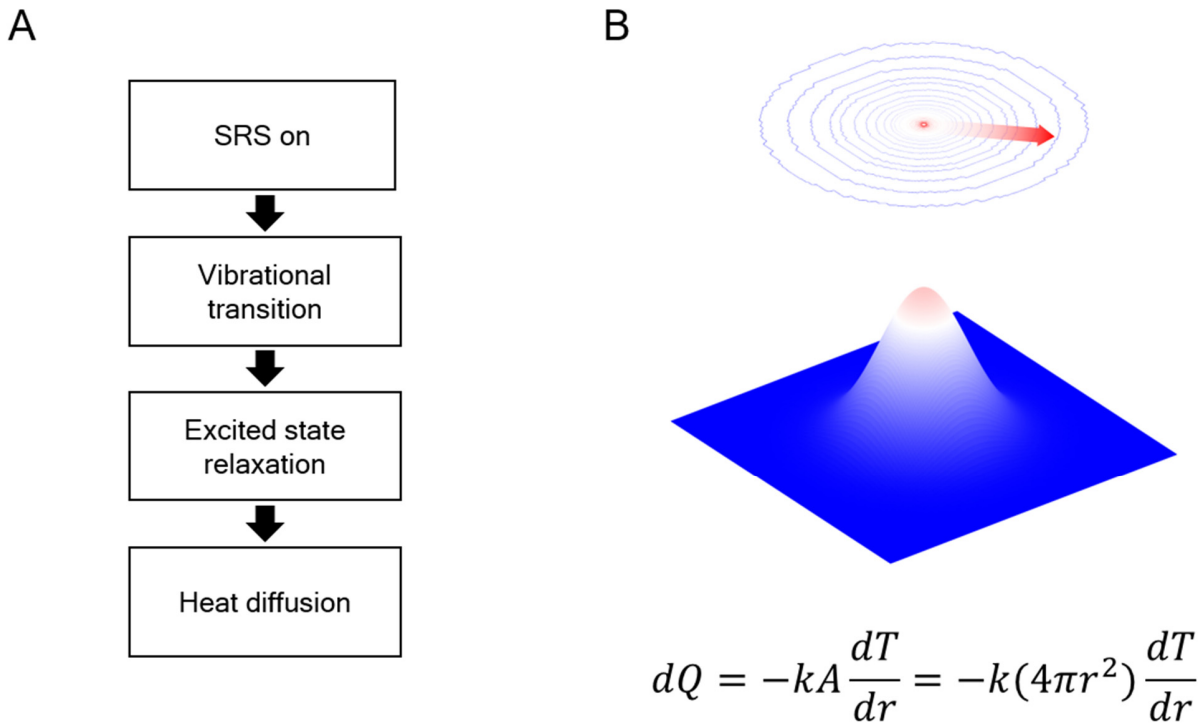

Fig. S1. Simulation modal for SRP induced thermal effect. (**A**) Thermal effect generation scheme. (**B**) Schematic of a heat diffusion model. The system is meshed into concentric spherical shells. Red arrow indicates the thermal propagation direction.

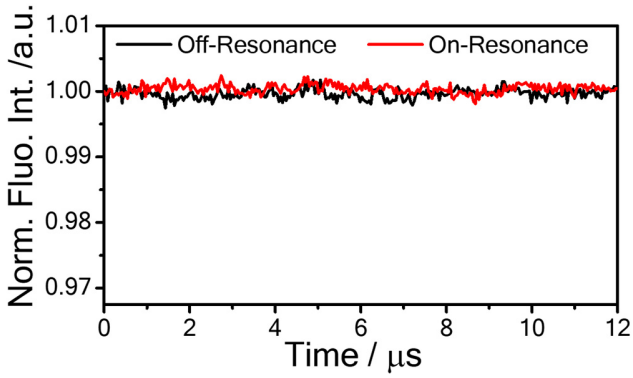

Fig. S2. Measured fluorescence of rhodamine 800 in DMSO during an SRS process. The beating frequency ($\omega_p - \omega_s$) was tuned to 2913 cm^{-1} for on-resonance and 2850 cm^{-1} for off-resonance.

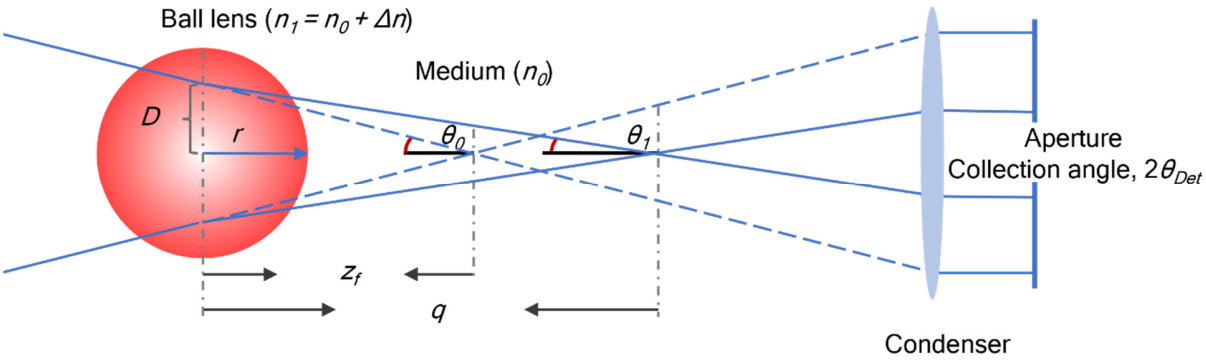

Fig. S3. Thermal ball lens model. The solid line indicates the propagation in the absence of a ball lens. The dashed line indicates the propagation of the probe laser in the presence of a ball lens. n_0 is the refractive index of the medium. Δn is the change of refractive index induced by the SRP effect.

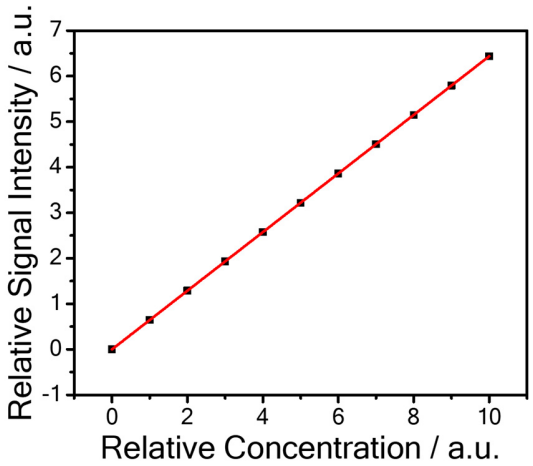

Fig. S4. Finite-difference time-domain simulation of SRP in high numerical aperture condition shows linear relationship between relative concentration and SRP signal intensity. Probe laser illumination numerical aperture: 1.47; collection numerical aperture: 0.4; simulation wavelength: 520 nm.

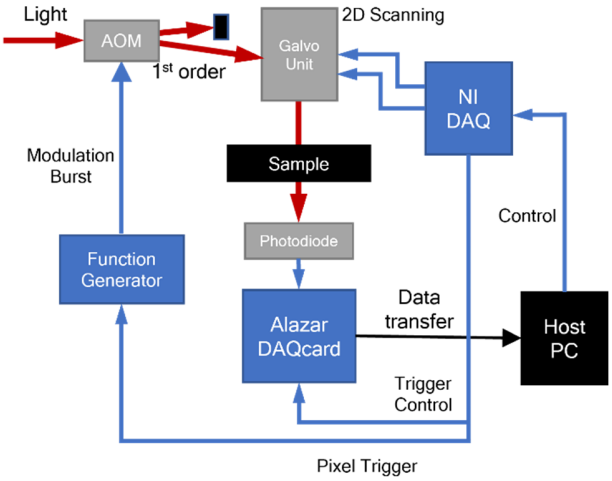

Fig. S5. Electronic control and data acquisition flow in the SRP microscope.

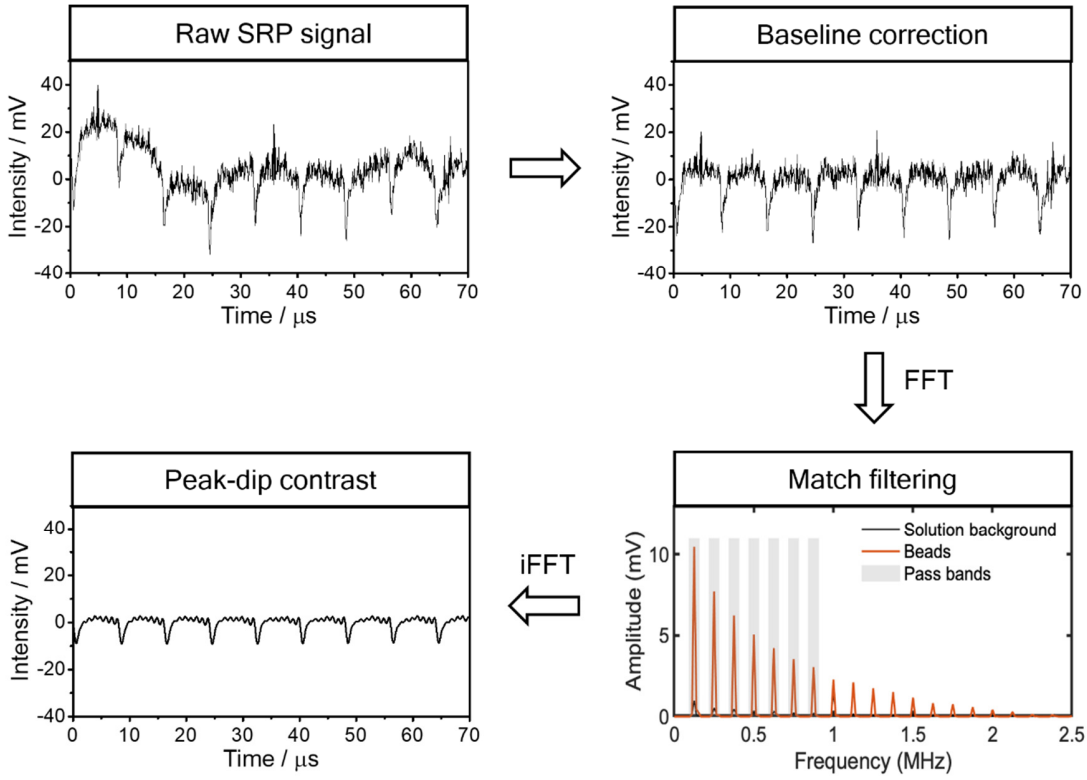

Fig. S6. Data processing of a thermal dynamic trace recorded by an SRP microscope. The signal is acquired from a single 100-nm PMMA nanoparticle at Raman shift of 2950 cm^{-1} immersed in glycerol-d8. FFT: fast Fourier transform; iFFT: inverse fast Fourier transform.

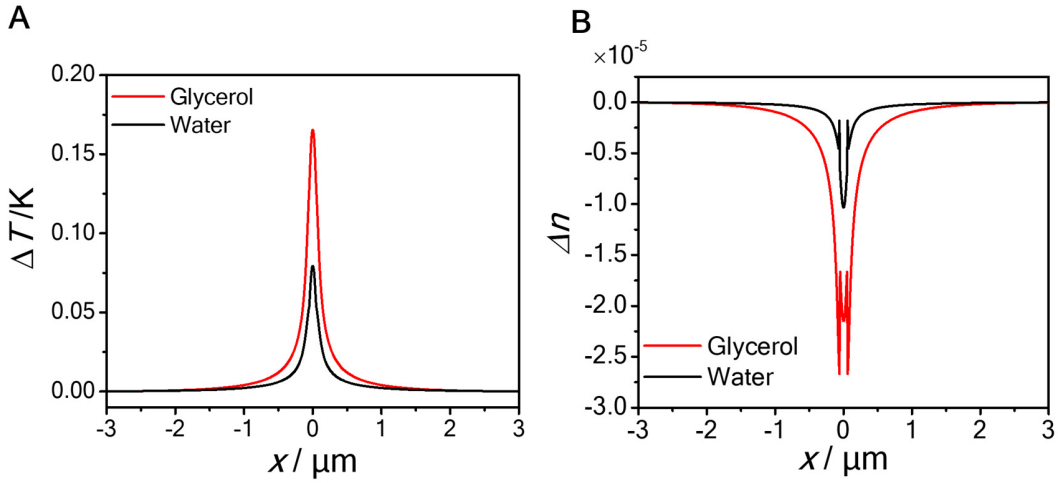

Fig. S7. Simulation results for the shape of temperature gradient (A) and thermal lens (B) induced by the SRS absorption of a 100-nm PMMA particle in glycerol or water. The PMMA particle is placed at x = 0. Two local minimums of refractive index change appear at two PMMA-medium boundaries, due to the sudden change of thermos-optic coefficients (*dn/dT*) at the boundaries.

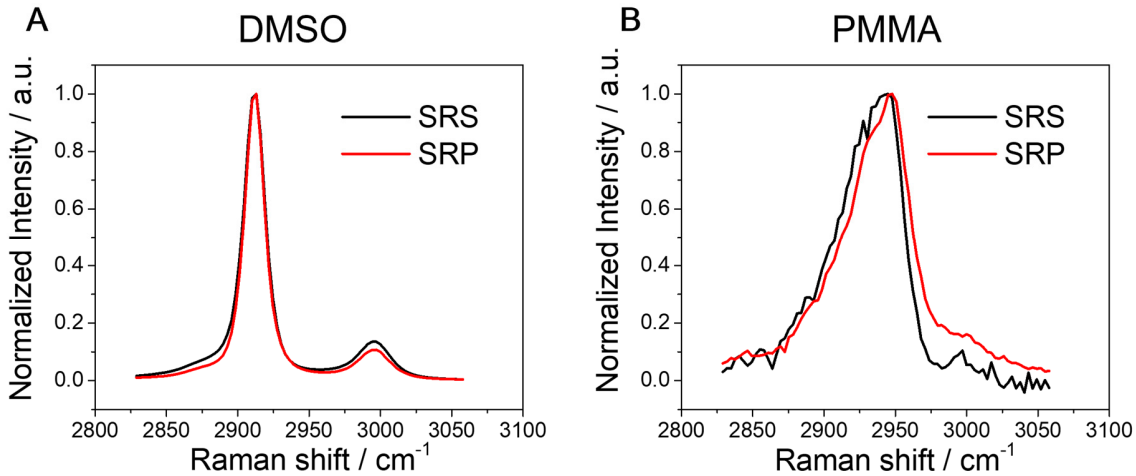

Fig. S8. SRP spectral fidelity. (**A**) Comparison between SRS and SRP spectra of pure DMSO. (**B**) Comparison between SRS and SRP spectra of a 500-nm PMMA particle.

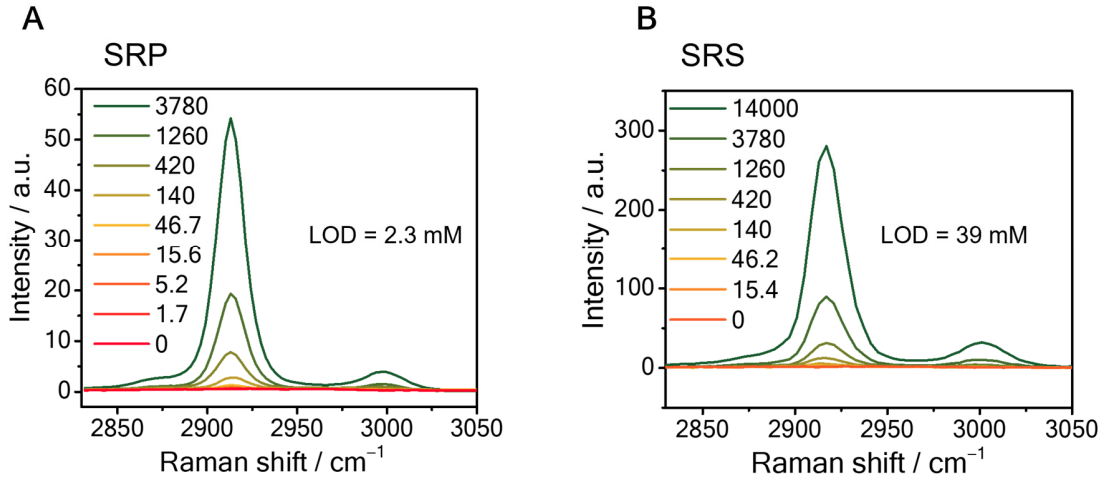

Fig. S9. Complete data set of LOD measurement of DMSO dissolved in DMSO-d6 with SRP (A) and SRS (B). Unit of concentration: mM.

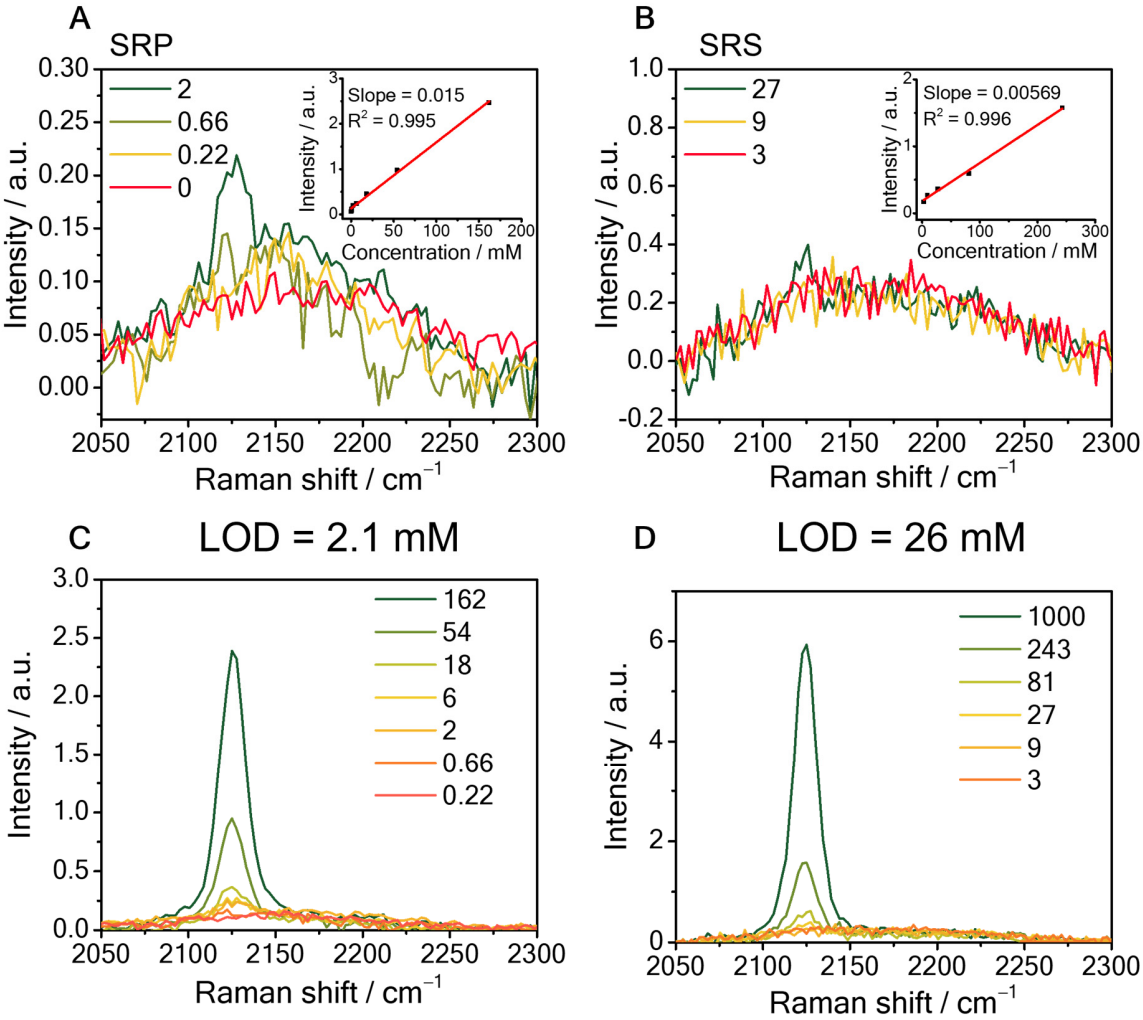

Fig. S10. Limit of detection (LOD) of SRP and SRS for 1,7-Octadiyne in DMSO. (**A**-**B**) SRP (**A**) or SRS (**B**) signal with a gradient concentration of 1,7-Octadiyne dissolved in DMSO. Insert shows the signal intensity as a function of concentration. (**C**-**D**) The complete data set of LOD measurement with SRP (**C**) and SRS (**D**). Unit of concentration: mM.

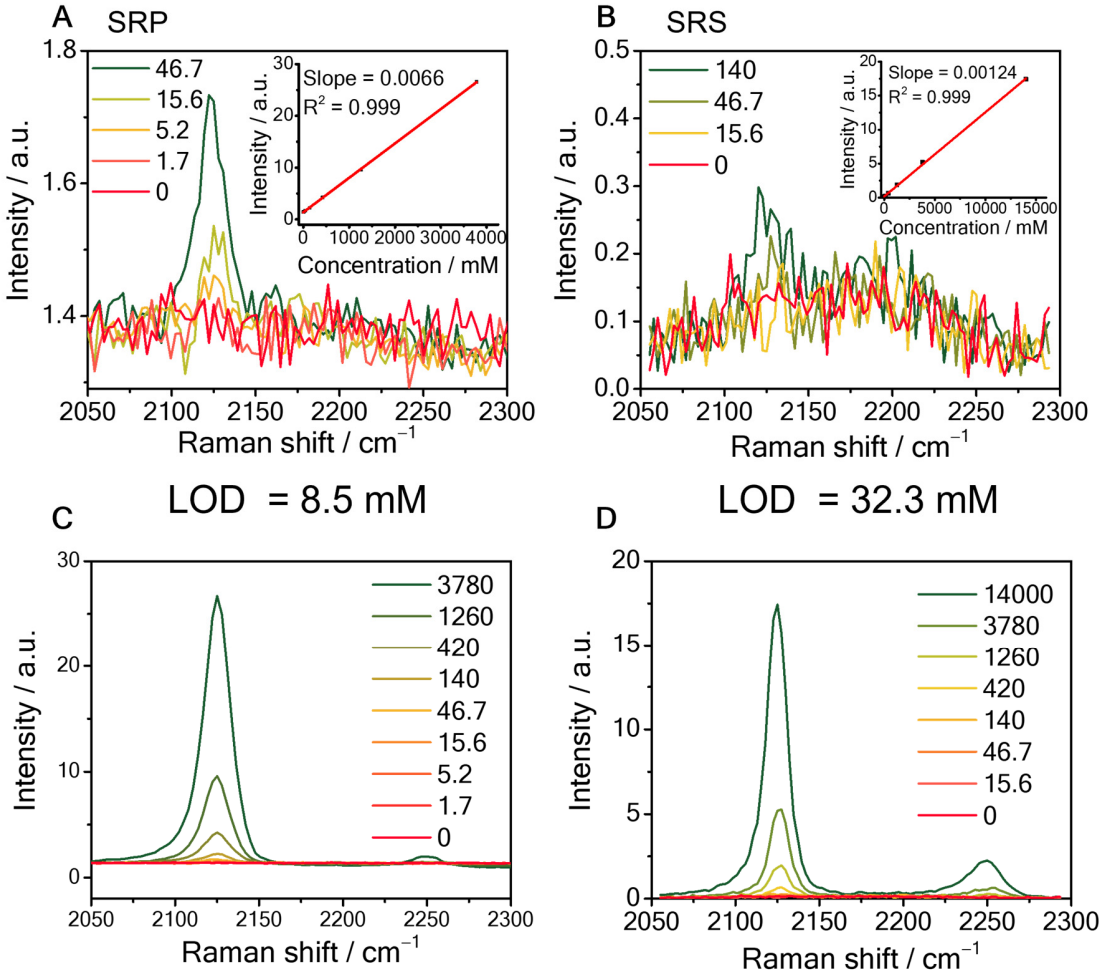

Fig. S11. Limit of Detection (LOD) of SRP and SRS for DMSO-d6 in DMSO. (**A-B**) SRP (**A**) or SRS (**B**) signal with a gradient concentration of DMSO-d6 dissolved in DMSO. Concentration unit: mM. Insert shows the signal intensity as a function of concentration. (**C-D**) The complete data set of LOD measurement with SRP (**C**) and SRS (**D**).

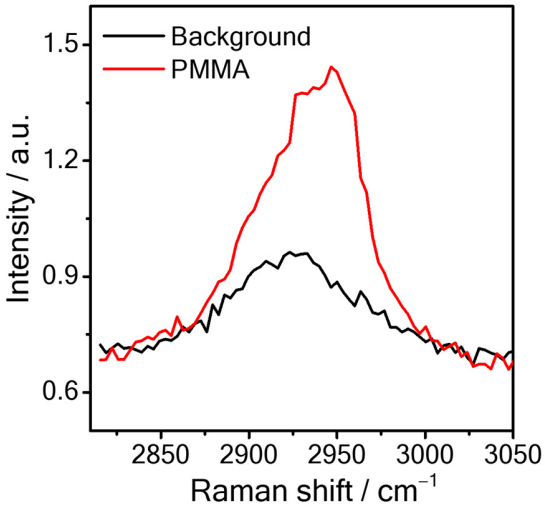

Fig. S12. SRP spectrum of a single 100 nm PMMA nanoparticle immersed in glycerol. The peak around 2950 cm^{-1} is from CH_3 stretching vibration in PMMA.

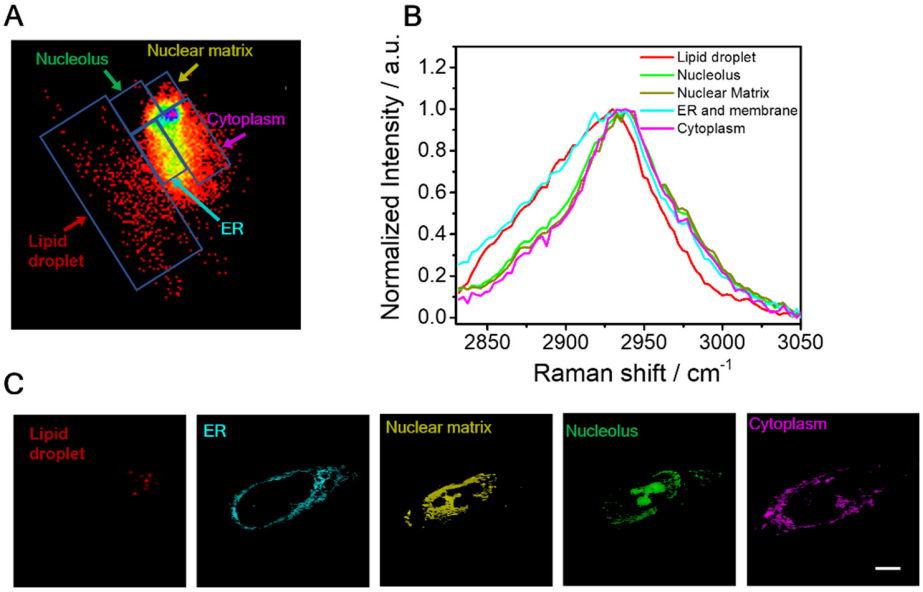

Fig. S13. Phasor analysis for the SRP image of SJSA-1 cells in aqueous environment. (**A**) Segmentation of the SRP image in the phasor domain. (**B**) The SRP spectrum at C-H region for each component. (**C**) Mapping of each component from phasor analysis. Scale bar: 10 μm.

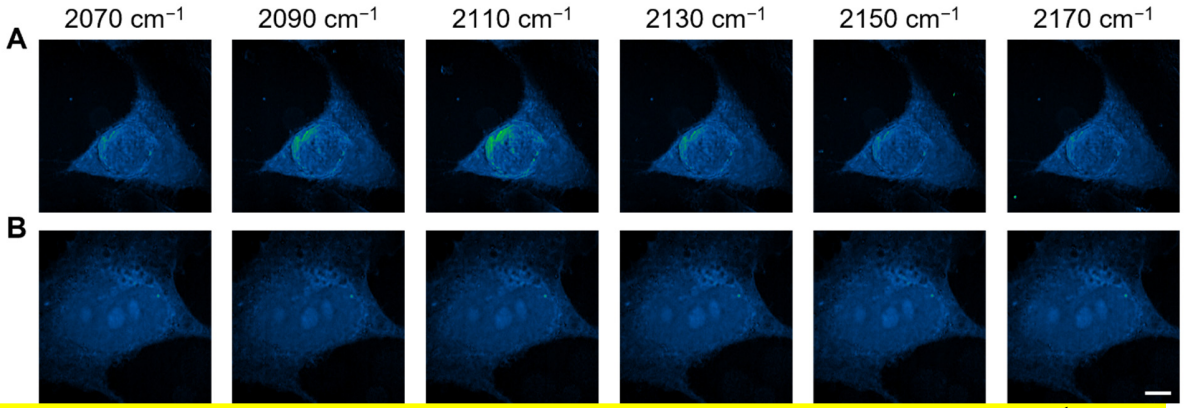

Fig. S14. Hyperspectral SRP imaging of SJSA-1 cell in PBS. Data were shown with 20 cm^{-1} spectral step. The cells were incubated with (**A**) or without (**B**) deuterated palmitic acid (PA-d31) for 18 h prior to imaging. Scale bar: 10 μm.

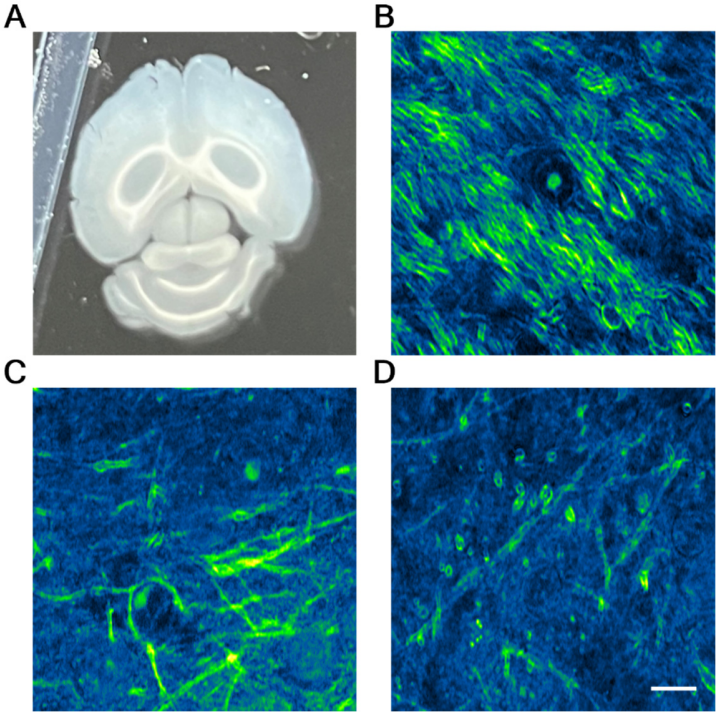

Fig. S15. SRP imaging of a mouse brain slice immersed in PBS. (**A**) Picture of the brain slice sample. (**B-D**) Representative SRP images of the brain slice sample at 2930 cm^{-1}. Scale bar = 12 µm.

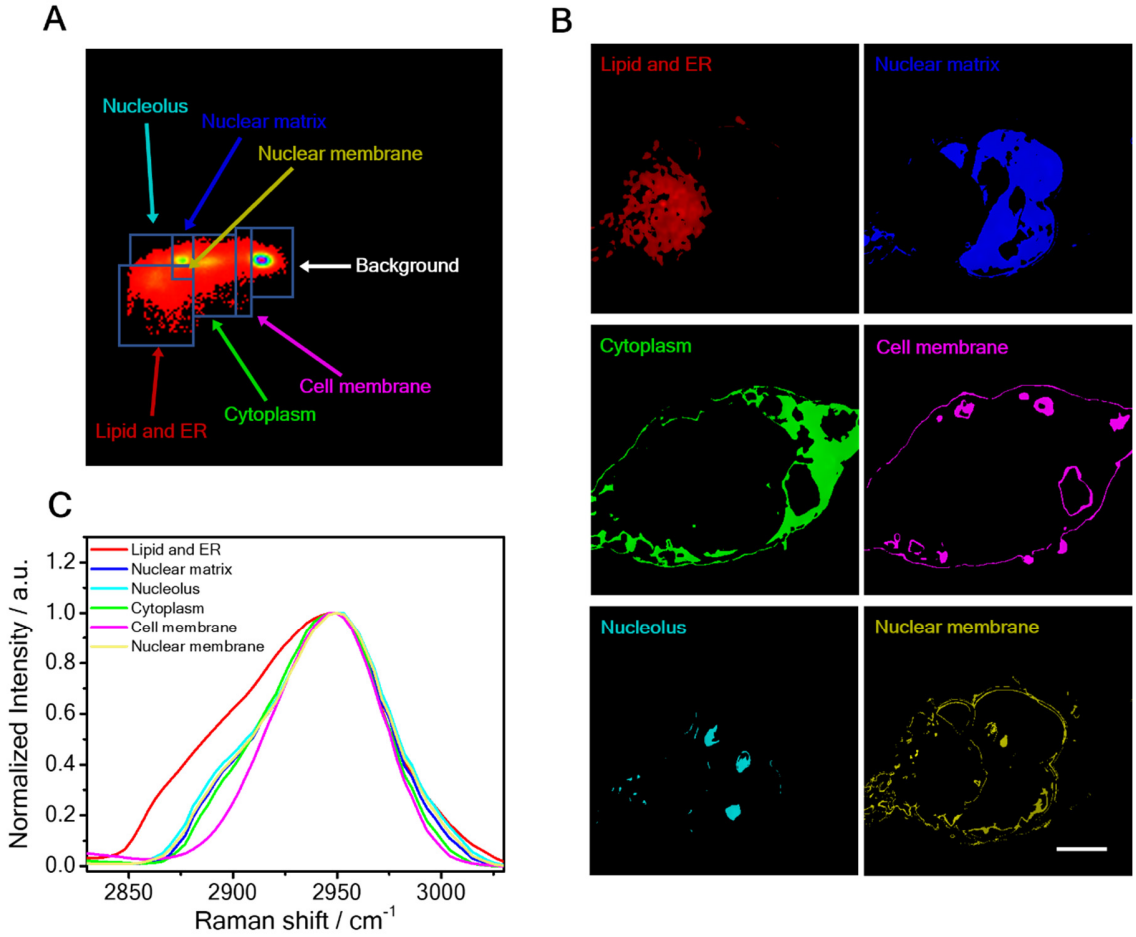

Fig. S16. Phasor analysis for the SRP image of glycerol-d8 immersed Mia PACA-2 cells. (**A**) Segmentation of the SRP image in the phasor domain. (**B**) Maps of each component from phasor analysis. Scale bar = 5 μm. (**C**) The SRP spectrum at C-H region for each component.

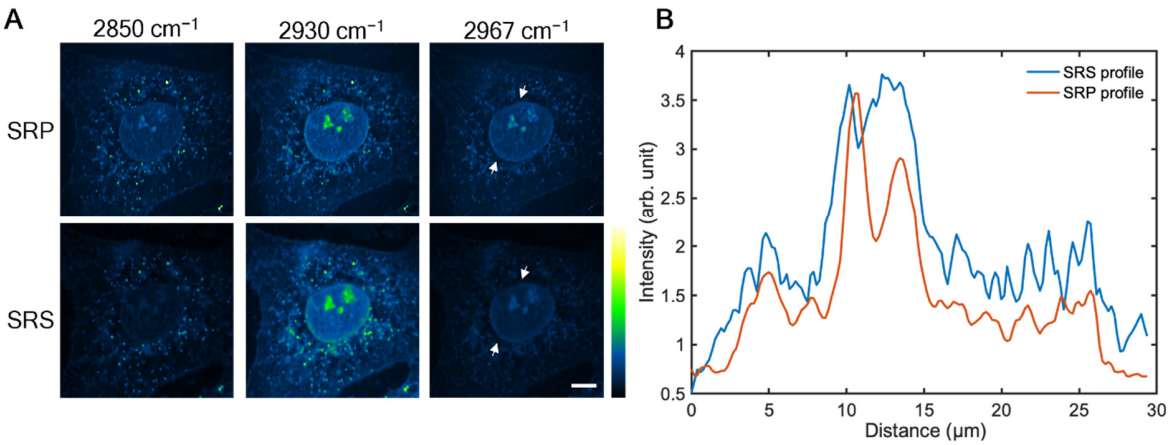

Fig. S17. Comparison between SRP and SRS images of SKOV3 cell immersed in glycerol-d8. (**A**) SRP and SRS images taken at three Raman shifts for lipid, protein and DNA. Scale bar: 10 μm. (**B**) The intensity profiles along the arrow-indicated lines in the SRP and SRS images at 2967 cm^{-1}.

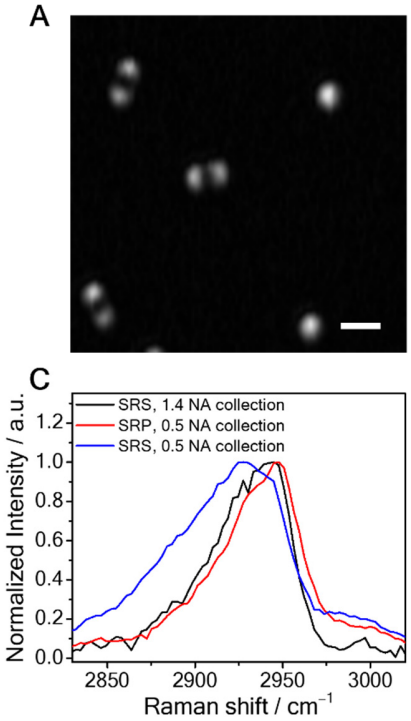

D

	Signal	BG	Noise	SBR	SNR
SRS	2.925	0.989	0.101	2.96	19.17
SRP	2.138	0.034	0.014	62.9	150.29

Fig. S18. Compare SRP and SRS performance under different light collection condition. SRP (**A**) and SRS (**B**) images of 500 nm PMMA nanoparticles recorded with 1.2 numerical aperture (NA) water objective for focusing and a 0.5 NA air condenser for signal collection. Raman shift: 2950 cm^{-1}. Scale bar: 1.5 µm. (**C**) Comparison between the SRP and SRS spectra of a single 500 nm PMMA nanoparticle. The broader line profile in SRS with low NA collection (blue line) is caused by a Raman-independent cross-phase modulation background. (**D**) Image quality comparison between SRP and SRS images. BG: background. SBR: signal to background ratio.

Thermal property	Unit	DMSO	hexane	glycerol	PMMA	water
Heat Capacity	J/(kg·K)	1966	2251	2400	1466	4184
Thermal conductivity	W/(m·K)	0.200	0.124	0. 283	0.167-0.25	0.598
Thermo-optic coefficient dn/dT (10^{-4})	K^{-1}	-4.93 [34]	-5.20 [51]	-2.30 [52]	-1.30 [53]	-1.13 [40]
Refractive index	-	1.479	1.375	1.473	1.492	1.333
Relative signal intensity	a.u.	8.37	8.29	3.21	2.93	1

Table S1. Thermal and thermo-optic properties and estimated relative signal intensity of the materials related to the study.

Movie S1. SRP imaging of lipid dynamics inside a living SJSA-1 cell. Frame rate: 2.8 s/frame. Scale bar: 5 µm.

Movie S2. Hyperspectral C-H SRP imaging of fixed SJSA-1 cell in aqueous environment. Scale bar: 10 µm.